



## RESEARCH ARTICLE

10.1002/2015JE004795

## Key Points:

- A new CTX-scale map details the geological history of Nili Patera
- Magmatism includes effusive basalts, magmatic intrusion, and ignimbrite(s)
- Volcanism and water suggest habitable environments in highland patera caldera

## Supporting Information:

- Figures S1 and S2
- Map S1

## Correspondence to:

P. Fawdon,  
peter.fawdon@open.ac.uk

## Citation:

Fawdon, P., J. R. Skok, M. R. Balme, C. L. Vye-Brown, D. A. Rothery, and C. J. Jordan (2015), The geological history of Nili Patera, Mars, *J. Geophys. Res. Planets*, 120, 951–977, doi:10.1002/2015JE004795.

Received 23 JAN 2015

Accepted 23 APR 2015

Accepted article online 28 APR 2015

Published online 26 MAY 2015

## The geological history of Nili Patera, Mars

P. Fawdon<sup>1</sup>, J. R. Skok<sup>2</sup>, M. R. Balme<sup>1</sup>, C. L. Vye-Brown<sup>3</sup>, D. A. Rothery<sup>1</sup>, and C. J. Jordan<sup>4</sup>

<sup>1</sup>Department of Physical Sciences, The Open University, Walton Hall, Milton Keynes, UK, <sup>2</sup>Department of Geology & Geophysics, Louisiana State University, Baton Rouge, Louisiana, USA, <sup>3</sup>British Geological Survey, Murchison House, Edinburgh, UK, <sup>4</sup>British Geological Survey, Nottingham, UK

**Abstract** Nili Patera is a 50 km diameter caldera at the center of the Syrtis Major Planum volcanic province. The caldera is unique among Martian volcanic terrains in hosting: (i) evidence of both effusive and explosive volcanism, (ii) hydrothermal silica, and (iii) compositional diversity from olivine-rich basalts to silica-enriched units. We have produced a new geological map using three mosaicked 18 m/pixel Context Camera digital elevation models, supplemented by Compact Remote Imaging Spectrometer for Mars Hyperspectral data. The map contextualizes these discoveries, formulating a stratigraphy in which Nili Patera formed by trapdoor collapse into a volcanotectonic depression. The distinctive bright floor of Nili Patera formed either as part of a felsic pluton, exposed during caldera formation, or as remnants of welded ignimbrite(s) associated with caldera formation—both scenarios deriving from melting in the Noachian highland basement. After caldera collapse, there were five magmatic episodes: (1) a basaltic unit in the caldera's north, (2) a silica-enriched unit and the associated Nili Tholus cone, (3) an intrusive event, forming a ~300 m high elliptical dome; (4) an extrusive basaltic unit, emplaced from small cones in the east; and (5) an extreme olivine-bearing unit, formed on the western caldera ring fault. The mapping, together with evidence for hydrated materials, implies magmatic interaction with subsurface volatiles. This, in an area of elevated geothermal gradient, presents a possible habitable environment (sampled by the hydrothermal deposits). Additionally, similarities to other highland volcanoes imply similar mechanisms and thus astrobiological potential within those edifices.

## 1. Introduction

Nili Patera (Figure 1) is a 50 km diameter caldera within the caldera complex at the center of the Syrtis Major Planum volcanic province. The caldera hosts a diverse range of landforms and a unique mineral assemblage, but the contextual history of these discoveries has not previously been holistically investigated. Syrtis Major Planum is a Hesperian-aged, low-angle volcanic shield located in the Martian highlands on the rim of the Isidis basin [Meyer and Grolier, 1977; Scott and Carr, 1978; Plescia and Saunders, 1979; Greeley and Guest, 1987; Tanaka et al., 2014a, 2014b] consisting of a gently sloping “shield” of lava plains 1100 km wide and estimated to have a mean thickness of 500 m [Hiesinger and Head, 2004]. Within the depression of the 200 km × 400 km central caldera complex are two separate calderas: Nili Patera to the north and Meroe Patera to the south [Hiesinger and Head, 2004; Plescia, 2004]. Volcanic activity within the calderas took place after the majority of Syrtis Major's development [Hiesinger and Head, 2004; Fawdon et al., 2013; Platz et al., 2014], between 2.04 and 3.02 Ga for Nili Patera and between 2.95 and 3.03 Ga for Meroe Patera [Robbins et al., 2011].

The elevation of the rim around Nili Patera is asymmetrical. There is ~1800 m of relief above the floor to the highest parts of the northwestern rim, whereas the southeast rim gently slopes up into the center of the central caldera complex (Figure 1) [Hiesinger and Head, 2004; Plescia, 2004]. The subsidence of the whole caldera complex has been linked to magma reservoir drainage and cooling [Kiefer, 2004; Dufek et al., 2014].

Orbital spectral data support the presence of variable mineralogy across the caldera floor. These variations are interpreted to be a consequence of differing compositions of erupted materials. The caldera floor shows evidence of the magmatic evolution, evidenced by differences in the chemistry of lavas of different ages. Christiansen et al. [2005] reported Thermal Emission Imaging System (THEMIS) observations that suggest a region of high silica concentration correlating to a bright cone and flow in the center of the caldera (now named Nili Tholus [http://planetarynames.wr.usgs.gov/Feature/15241?\\_\\_fsk=1208884113](http://planetarynames.wr.usgs.gov/Feature/15241?__fsk=1208884113)), as well as regions of distinct thermal properties, inferred to be bedrock. These exposed bedrock parts of the caldera floor are considered by Clenet et al. [2013] to have a large olivine component and are distinct from

©2015. The Authors.

This is an open access article under the terms of the Creative Commons Attribution License, which permits use, distribution and reproduction in any medium, provided the original work is properly cited.

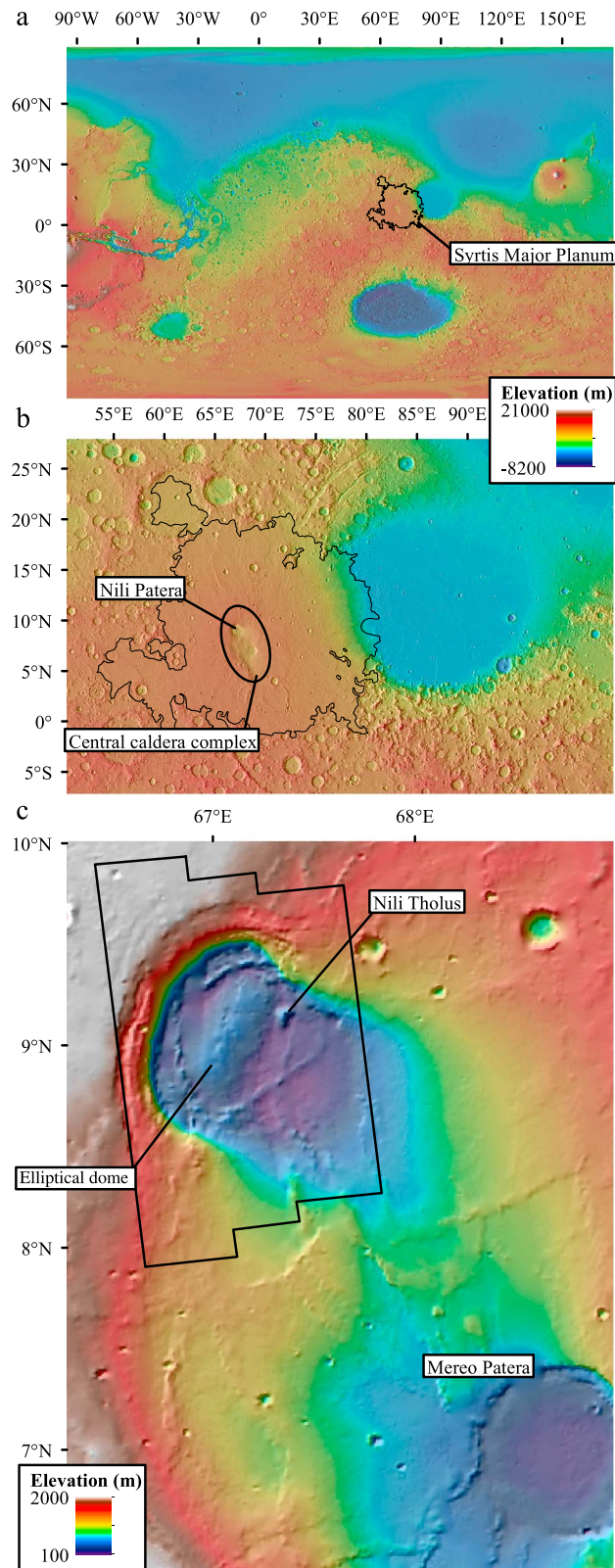


**Figure 1.** Location of study area. (a) MOLA topography overlain on hill-shaded MOLA topography showing the extent of Syrtis Major Planum delimited by the black line within the eastern hemisphere of Mars [Tanaka et al., 2014]. (b) Syrtis Major Planum; the ellipse indicates the area of the central caldera complex/depression. (c) Close-up of the caldera region; the CTX mosaic study area is outlined in black. The background is MOLA topography overlain on hill-shaded MOLA topography.

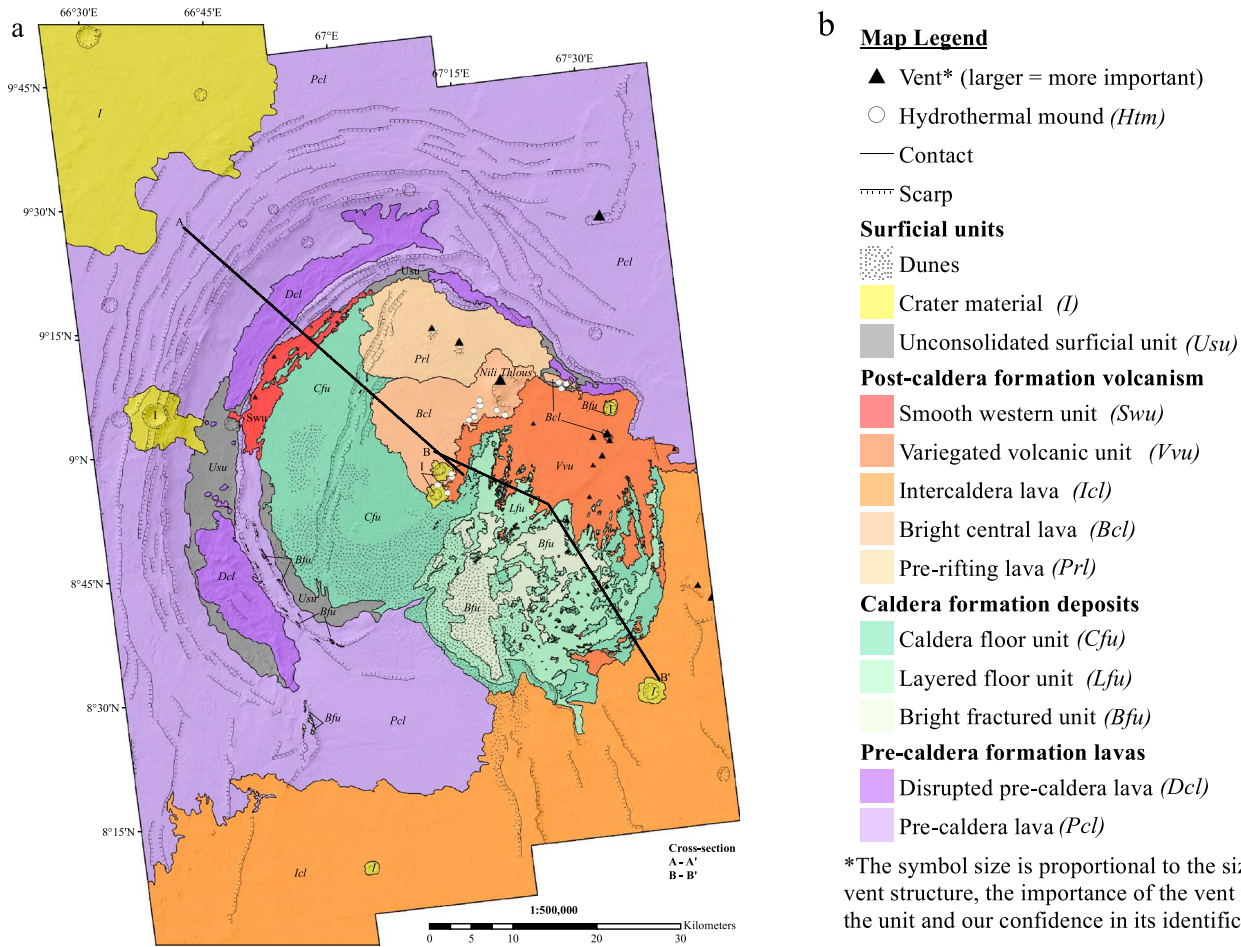


**Figure 2.** Geological units and surface features in and around Nili Patera. (a) Geomorphological surfaces and features and inferred geological units for Nili Patera. The geological structure is summarized in Figure 4. (b) Key to units and map symbols. Also, see supporting information.

areas of the caldera floor identified by *Wray et al.* [2013] to be fractured bedrock enriched in feldspar relative to mafic minerals. Because different spectral units reflect various physical properties of the volcanic material, we consider these differences to be differences in the primary volcanic material. In addition to variations in primary lithology, *Skok et al.* [2010a] identified deposits of amorphous silica situated on Nili Tholus, leading to the suggestion that these features have a hydrothermal origin, the first, and to date only, such deposits to be discovered within a Martian caldera.

The aim of this work is to understand the history of Nili Patera. We have produced a new geological map (Figure 2) that compiles the spatial, structural, and stratigraphic relationships between magmatic evolution, hydrothermal activity [*Christensen et al.*, 2005; *Skok et al.*, 2010a; *Wray et al.*, 2013], and new observations of the caldera’s geomorphology. Using this map, we detail the history of Nili Patera. First, we investigate the formation mechanism of Nili Patera and the emplacement/exposure of caldera floor basement materials. Second, we investigate the volcanotectonic evolution of the caldera floor, the implications of intrusive activity, magma evolution, and the setting of hydrothermal deposits. Third, we consider the implications of this work for calderas associated with other Martian highland volcanoes.

## 2. Data and Methods

Our map (Figures 2 and 3 and supporting information) uses three Mars Reconnaissance Orbiter [*Zurek and Smrekar*, 2007] Context Camera (CTX) [*Malin et al.*, 2007] digital terrain models (DTMs) and orthorectified images from three CTX image pairs as base layers. High Resolution Imaging Science Experiment (HiRISE)

Stratigraphy

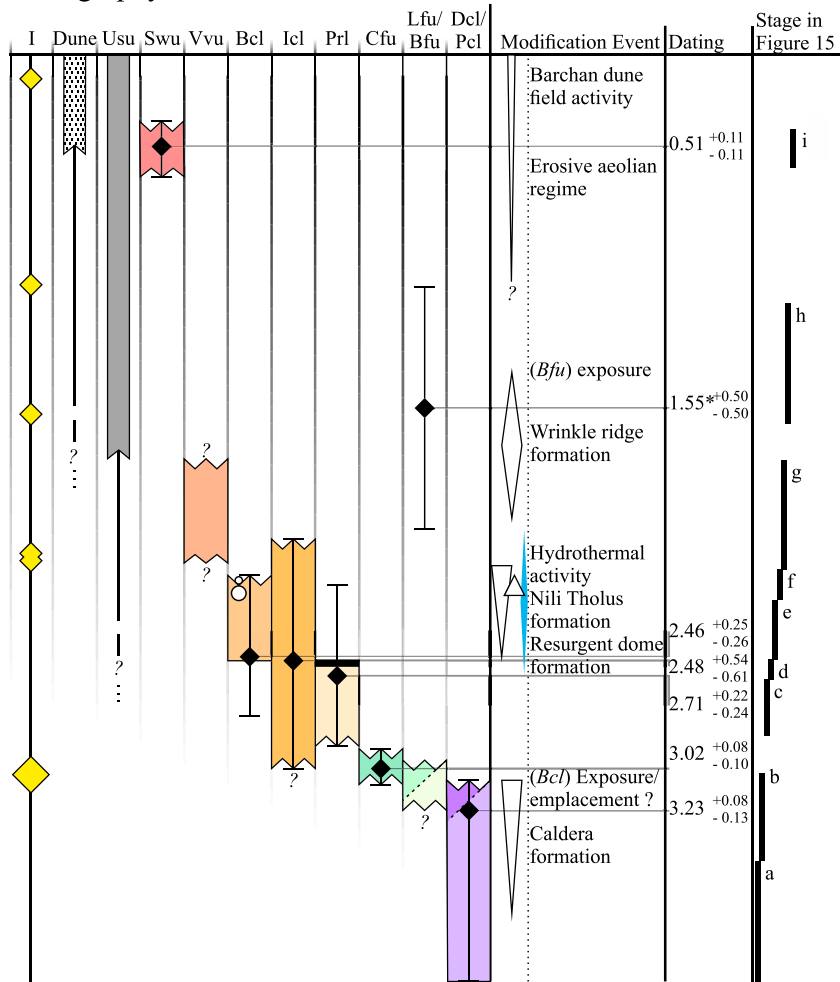


**Figure 3.** Inferred stratigraphic history of Nili Patera: units are arranged in stratigraphic order. The size of colored bars and modification event diamonds indicate the relative duration of the events and the approximate time period during which they took place. Dates and error bars shown are from Table 1 including asterisk taken from Robbins *et al.* [2011].

[McEwen *et al.*, 2007] data have been used where available for detail, and High Resolution Stereo Camera (HRSC) [Neukum *et al.*, 2004] data were used to supply color information to the other higher-resolution data products. For mapping, we used the commercially available ArcGIS 10.1 software, combined with the GeoVisionary 3D visualization environment developed by the British Geological Survey for visualizing large 3D data sets. This is fully interactive with ArcGIS 10.1, allowing unit and contact mapping to be performed in 3D.

**2.1. Topography and Visual Analysis**

**2.1.1. CTX Images and DTM Generation**

We generated a mosaic of three digital elevation models (DTMs) from six CTX images (G04\_019740\_1890\_XN\_09N293W, G04\_019595\_1890\_NX\_09N292W, B20\_017617\_1891\_XI\_09N292W, G01\_018606\_1891\_XI\_09N292W, G01\_018672\_1890\_XI\_09N293W, and B21\_017828\_1890\_XI\_09N293W) using the method of Kirk *et al.* [2008]. This method uses public domain Integrated Software for Imagers and Spectrometers software to preprocess the raw experimental data records before processing in SocetSet®, a commercially available photogrammetry suite (<http://www.socetset.com>). During the processing in SocetSet®, we controlled the DTMs using MOLA (Mars Orbital Laser Altimeter) track data [Smith *et al.*, 2001], thus allowing us to correlate elevations between DTMs of different scales. The output

from SocetSet® was an 18 m/pixel DTM. Additionally, the DTM was used to orthorectify three CTX images: G04\_019740\_1890\_XN\_09N293W, B20\_017617\_1891\_XI\_09N292W, and G01\_018672\_1890\_XI\_09N293W. After manual georeferencing of G04\_019740\_1890\_XN\_09N293W and B20\_017617\_1891\_XI\_09N292W to image G04\_019740\_1890\_XN\_09N293W, these images form the visual and topographic base layers of the map. All other data have been georeferenced to this layer.

#### 2.1.2. HRSC and HiRISE Images

To complement the CTX base layer, all HiRISE images publicly available at the time of writing were imported into the geographic information system and examined. We have also studied HiRISE DTMs DTEEC\_017762\_1890\_018039\_1890\_A01 and DTEED\_013582\_1890\_020940\_1890\_A01 ([http://hirise.lpl.arizona.edu/dtm/dtm.php?ID=ESP\\_013582\\_1895](http://hirise.lpl.arizona.edu/dtm/dtm.php?ID=ESP_013582_1895), [http://hirise.lpl.arizona.edu/dtm/dtm.php?ID=ESP\\_017762\\_1890](http://hirise.lpl.arizona.edu/dtm/dtm.php?ID=ESP_017762_1890)) and a DTM made by ourselves from a stereo pair ESP\_035247\_1890 and ESP\_035537\_1890 using SocetSet. HiRISE data do not provide complete coverage of the mapped area but do add detailed textural information to units mapped in CTX. We used HRSC data record H1098\_0000 to provide RGB color. The RGB color components (h1089\_0000\_re3, h1098\_0000\_gr3, and h1089\_0000\_bl3) were composited using tools within ArcGIS 10.1, georeferenced to the orthorectified CTX base map, and then pan-sharpened using CTX images G04\_019740\_1890\_XN\_09N293W and B20\_017617\_1891\_XI\_09N292W.

#### 2.1.3. Compact Remote Imaging Spectrometer for Mars Composition Analysis

The primary compositional data used in this paper are observations from the Compact Remote Imaging Spectrometer for Mars (CRISM) visible/near-infrared hyperspectral imaging instrument [Murchie *et al.*, 2007]. CRISM acquires Full-Resolution Targeted (FRT) images at 18 m/pixel spatial resolution using 544 spectral bands ranging from 362 to 3920 nm. CRISM observations have been corrected for instrumental artifacts and converted into  $I/F$  ratios where  $I$  is the radiance at sensor and  $F$  is the solar irradiance at the top of the Martian atmosphere divided by  $\pi$  [Murchie *et al.*, 2007]. To use the observations for surface mineral measurements, we used a simple multiplicative correction to remove the atmospheric contribution to the spectra. This was determined using a volcano scan method developed and tested on the Imaging Spectrometer for Mars [Bibring *et al.*, 1989] and Observatoire pour la Minéralogie, l'Eau, les Glaces et l'Activité [Mustard *et al.*, 2005]. A detailed description of the volcano scan method is provided by McGuire *et al.* [2009].

#### 2.1.4. Surface Age Estimates

To estimate emplacement ages for some of the mapped surfaces, we employed impact crater size frequency statistics. We identified impact craters by eye in CTX images or HiRISE images and digitized them in ArcGIS using the three-point digitization method in the CraterTools software package [Kneissl *et al.*, 2011] guided by the methodologies of Platz *et al.* [2013] and Tanaka *et al.* [2014b]. Units were crater counted after they had been identified stratigraphically. Care was taken not to count craters embayed by the units being examined; craters in all states of degradation were counted to sample formation age rather than a resurfacing age. The following units were not sampled for crater counting: the disrupted caldera lavas (*Dcl*), variegated volcanic unit (*Vvu*), bright fractured unit (*Bfu*), and the layered floor unit (*Lfu*). Those units displayed significant evidence of crater modification, ongoing erosion, or other resurfacing processes and so were deemed unsuitable for crater counting. To determine crater retention model ages, we used the Craterstats software package [Michael and Neukum, 2010]. We considered the whole cumulative population and then fitted ages using the Hartman 2004 production and chronology function to the steepest part of the slope. For consistency between units, we endeavored to use the same crater size bins for units counted on directly comparable data for determination of model ages. Crater size frequency model ages are summarized in Table 1. Additionally, we note that the conclusions of Warner *et al.* [2015] appreciating the implications for validity consider the model ages over areas  $<1000 \text{ km}^2$ .

### 3. Observations

The primary output of our observations is a map, a summarized version of which is presented at 1:250,000 scale in the supporting information to this article and in Figure 2 at a scale of 1:500,000. Geologic units (Figures 2 and 3) and structure overlain on topography (Figure 4) are also presented. We characterized units at the highest available resolution on a geological and geomorphological basis, depending on the availability of derived mineralogy, and then mapped onto the CTX base layer.

**Table 1.** Crater Count Summary<sup>a</sup>

Unit	No. Craters Counted	Area ( $\times 10^2$ km <sup>2</sup> )	Size Range Fitted (m)	No. Craters in Fitted Range	Model Age (Ga)	
<i>Pcl</i>	1429	18.5	350–1500	117	3.23 (+0.08, –0.13)	Formation
			20–450	522	2.54 (+0.10, –0.10)	Resurfacing <sup>b</sup>
<i>Bfu</i> <sup>c</sup>					1.55 (+0.50, –0.50)	Resurfacing <sup>d</sup>
<i>Cfu</i> <sup>e</sup>	2166	0.88	90–450	495	3.02 (+0.13, –0.22)	Formation
<i>Prl</i>	734	1.21	150–550	116	2.71 (+0.22, –0.24)	Formation
<i>lcl</i>	480	1.51	480–1500	16 <sup>f</sup>	2.48 (+0.54, –0.61)	Formation
<i>Bcl</i>	312	1.17	150–550	63	2.46 (+0.25, –0.26)	Formation <sup>g</sup>
<i>Swu</i>	190	0.51	110–300	22 <sup>f</sup>	0.51 (+0.11, –0.11)	Formation

<sup>a</sup>Summary of input data and crater size frequency model derived ages (full description in the supporting information). All counts used CTX data unless noted otherwise.

<sup>b</sup>Aeolian redistribution of impact ejecta and pyroclastic material.

<sup>c</sup>Data taken from *Robbins et al.* [2011] for comparison.

<sup>d</sup>Determined by stratigraphy; small numbers of craters and crater remnants.

<sup>e</sup>HIRISE data were used for crater counting.

<sup>f</sup>These counts are too small to be confident in their reliability.

<sup>g</sup>This count did not include the two large craters in the south of the unit. These were excluded because we considered them to be outliers that biased the age determination when included.

### 3.1. Physiography

Nili Patera can be split topographically into four areas, as can be seen on Figure 4, which shows the topography of Nili Patera from the CTX DTM mosaic. The northwest area, to the left of the solid white line and external to the dashed ellipses in Figure 4, includes the arcuate edge of the caldera, where the terrain drops by ~1700 m to the foot of the interior scarps. The boundary with the western caldera floor is a double-ridged cliff that is ~20 m high in the middle but rises to ~250 m high at either end. The second area, the western caldera floor (left-hand dashed ellipse in Figure 4), is a domed elliptical region that rises to ~400 m at its highest point. The crest, trending north-northeast to south-southwest, is split by an axial graben along the same trend. Nili Tholus lies on the boundary between the third area—the eastern caldera floor—and the western caldera floor. Nili Tholus reaches ~630 m above the surrounding caldera floor to 763 m in elevation at its peak. The eastern caldera floor, at ~200 to ~60 m MOLA elevation, is crosscut by a conjugate pair of wrinkle ridges intersecting at 120° that are 35–50 m higher than the surrounding caldera floor. The north-south trending wrinkle ridge is poorly expressed south of the intersection (Figure 4) but becomes clear again nearer the margin of the eastern caldera floor. Southeast of the solid white line in Figure 4 is the fourth area, the zone between Nili and Meroe Patera. This area reaches 700 m in elevation at the southern extent of the mapped area and is demarcated by a change in surface roughness and slope outside of the caldera floor. This area also hosts ridges longitudinally bounded by faulting with a convex cross section that is commonly interpreted to be indicative of compressional features [*Plescia and Golombek*, 1986]. Here, the ridges have ~125 m of relief along the axis of the central caldera complex.

### 3.2. Geologic Units

Here we subdivide the region into units on the basis of their spectral and textural characteristics. Using this, along with stratigraphic and inferred genetic associations, we group and derive interpretation for the units. An overview of each unit's description is presented here; fuller unit descriptions can be found in the supporting information.

We have identified 13 units (Figure 2) in the mapped area and have divided these into four groups based on their geological and stratigraphic relationships (Figure 3 and Table 1). The unit and group names are not intended to follow U.S. Geological Survey unit names for global or regional maps of this area but are presented in the context of this paper only. For orientation, Figure 5 shows the locations of subsequent figures in the result section, as well as locations with CRISM coverage.

#### 3.2.1. Caldera External Lavas

Caldera external lavas are units outside the Nili Patera floor emplaced prior to the structural development of Nili Patera (Figure 6). Vent structures, faulted flow margins, and layering exposed by caldera-centric normal faulting are observed. Precaldera lavas (*Pcl*) are fractured into angular to tabular blocks forming the

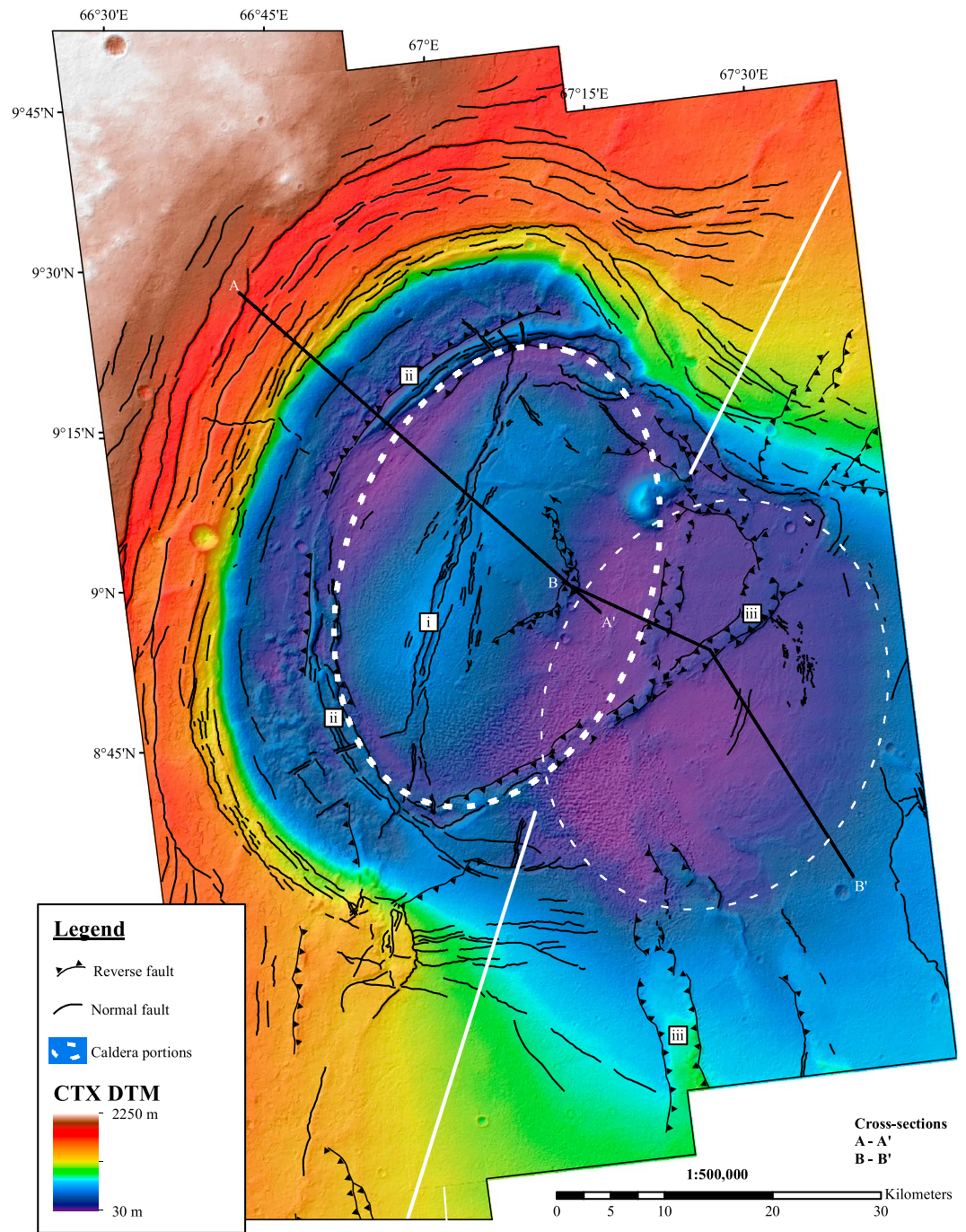


**Figure 4.** Structure and topography of Nili Patera, as shown by a mosaicked CTX colored DTM and hill shade. The DTM has a pixel size of 18 m. Structural mapping symbols are shown in the legend. Dashed lines show the two areas of the caldera floor, while solid white lines indicate approximate boundaries of different areas outside the caldera floor as described in the text. Also identified are (i) the resurgent dome (lighter blue area), (ii) interior circumferential caldera ridges, and (iii) “wrinkle ridges” aligned along the trend of the central caldera complex floor.

disrupted precaldera lava unit (*Dcl*) at the base of the caldera collapse faults. The surface between these blocks is filled by unconsolidated surficial materials (*Usu*). Other areas are formed of rubbly mounds with occasional very bright outcrops reminiscent of the bright fractured unit (*Bfu*) described below. The surface between the mounds is a smooth and fine-grained (i.e., with few features at HiRISE resolution) material.

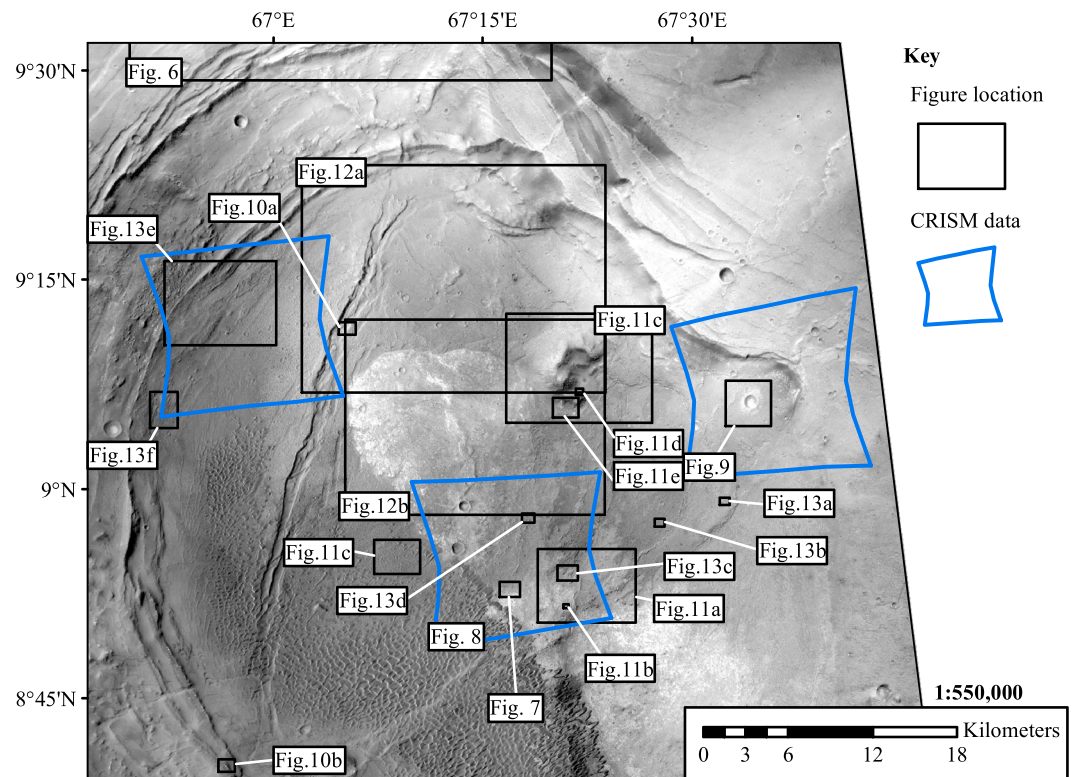


**Figure 5.** Contextual summary of locations for Figures 6–11. The locations of the CRISM FTR data used in this study are also shown. Background is a CTX orthoimage mosaic from (left to right) G04\_019740\_1890\_XN\_09N293W, G04\_019740\_1890\_XN\_09N293W, and B20\_017617\_1891\_XI\_09N292W.

### 3.2.2. Caldera-Forming Deposits

Caldera-forming deposits formed contemporaneously with, to shortly after, the caldera formation event. The bright fractured unit (*Bfu*) at the base crops out primarily in the eastern caldera floor. It appears almost white in CTX images, and in HiRISE data, it has a homogenous smooth surface with a massive internal structure comprised of high- and low-centered polygonal and rectilinear fractures, 4–5 m across. Subhorizontal, discontinuous layers exposed by erosion indicate layer-like fracture planes (Figure 7). Previously, *Christensen et al.* [2005] identified this area as bedrock. Spectrally, the bright fractured material exhibits a broad electronic absorption centered at 1.2  $\mu\text{m}$  (yellow in Figure 8b). This spectroscopic signature, of a band easily masked by the spectra of other iron magnesium silicates, is consistent with a relatively pure exposure of plagioclase with  $\sim 0.1$ –1% FeO [*Wray et al.*, 2013]. The clarity implies  $< 5\%$  of the rock is made of Fe silicates and that  $> 95\%$  is made from plagioclase and other undetected silica-rich phases such as quartz [*Cheek et al.*, 2013; *Horgan*, 2013]. However, thermal infrared measurements [*Rogers and Nekvasil*, 2015] seem to rule out felsic interpretations. There are three other outcrops ascribed to this unit: first, in CRISM image FRT0000B80F, the key spectral signature is seen in the ejecta of a  $\sim 1100$  m diameter crater (Figure 9), confirming that the unit is present to a minimum depth of  $\sim 100$  m. Second, boulder fields of characteristically bright, 2–8 m wide boulders (Figure 10) can be seen eroding out from walls in the eastern caldera floor dome axial graben. Finally, high-albedo friable outcrops occur along crests of the double-ridged cliffs, within the disrupted block unit and at the edges of faulted massifs at the caldera margin (Figure 10). This last example could be the same material, on the basis of the very high albedo and common stratigraphic position prior to fault movement, or unrelated.

The upper contact with the layered floor unit (*Lfu*; see below) is gradational and poorly defined, but the units are differentiated in two key ways. First, where the brightest material is covered by patchy outcrops of darker-toned material (*Lfu*), there is gradual change in spectral response as this overlying material thickens and becomes more continuous, masking the spectral signature. Second, there is a textural progression in form from

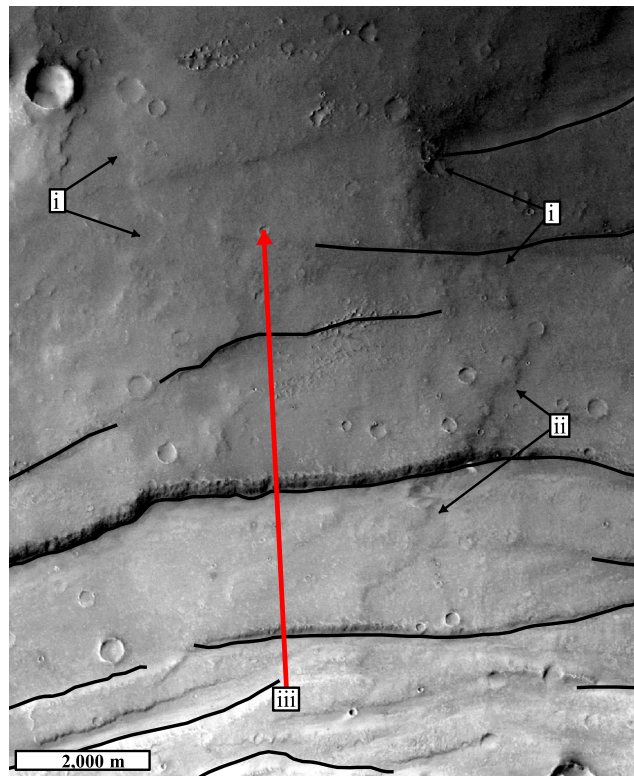


**Figure 6.** A north-south trending lava flow that was emplaced before caldera formation-associated faulting. (i) Edges of the large lava flow (black arrows), (ii) caldera-centric normal faults (black lines), and (iii) the downhill direction of flow prior to caldera collapse (red arrow). The crosscutting relationship shows that the flow formed before the caldera collapse faulting.

contiguous layering toward surfaces featuring regular polygonal patterns of fractures. These relationships, which often appear gradational, can be used to infer that the units could be genetically related.

Above this contact is the layered floor unit (*Lfu*). The layers have a smooth surface which is crosscut by a semi-regular to rectilinear network of subrounded fractures (Figures 7 and 11a), and erosional windows show some fractures running through both units. Above this surface, the texture becomes rubby. Spectral data show this unit to be characterized by more “red” colors in the RGB image (Figure 8). Where the unit is patchy on a scale smaller than that of CRISM pixels (Figures 7b), the spectral response is evidently mixed with that of the distinctive underlying bright fractured unit.

The remainder of the caldera floor (crater floor unit; *Cfu*) has a rough, undulating, pitted surface made of angular boulders and rubble. Between these clasts are aeolian sediments that infill fractures

(Figure 11c). All the unit boundaries are obscured by subsequent deposits or surficial material. In the east, the top surface of the unit is missing in the stratigraphy, except where sections are exposed on wrinkle ridges. Identification of this unit is correlated to the surface in the western region by HiRISE observations. Christensen [2005] also established that this unit occurs in both sides of the caldera.

### 3.2.3. Postcaldera Formation Volcanism

Postcaldera formation volcanism occurred after the emplacement of the caldera floor. The first of these units comprises lavas emplaced prior to uplift and rifting by the resurgent dome (*Prf*). The unit has ~20 m of relief above the caldera floor unit (*Cfu*), and, toward the center, are several irregular flat mounds with tuya-like tops ~20 m high (Figure 12a). The surface is mid-grey in tone, with smooth mantling material obscuring the detailed texture.

The second volcanic unit (bright central lava unit; *Bcl*) is situated close to the center of the caldera. The unit was emplaced contemporaneously with the initiation of faulting related to the domed portion of the western caldera floor (Figure 4) but prior to the main uplift phase of this resurgent dome (Figure 12b) and now dips ~1.4° east. The unit is formed of lava of a composition enriched in silica, as inferred from its thermal characteristics and albedo [Christensen *et al.*, 2005]. This interpretation is supported by a lobate perimeter with 30–40 m of relief—observations indicative of relatively high-viscosity flows, commonly associated with lava compositions enriched in silica. The unit overlies faults parallel to the (now uplifted) resurgent dome axis. The surface is light toned with a patchy covering of darker material. This mantling material is not seen inside the unit where excavated by two impacts. To the southeast, the unit does not have a clear topographic boundary. The edge is overlapped by later, post-western caldera floor doming units, obscuring the topographic expression of the original extent. Two outliers share the unit’s thermal characteristics [Christensen *et al.*, 2005]: the first is of unclear origin but hosts bright mounds indicative of the hydrothermal sinter [Skok *et al.*, 2010a]. The second, with a flat top and irregular perimeter, is overlapped by

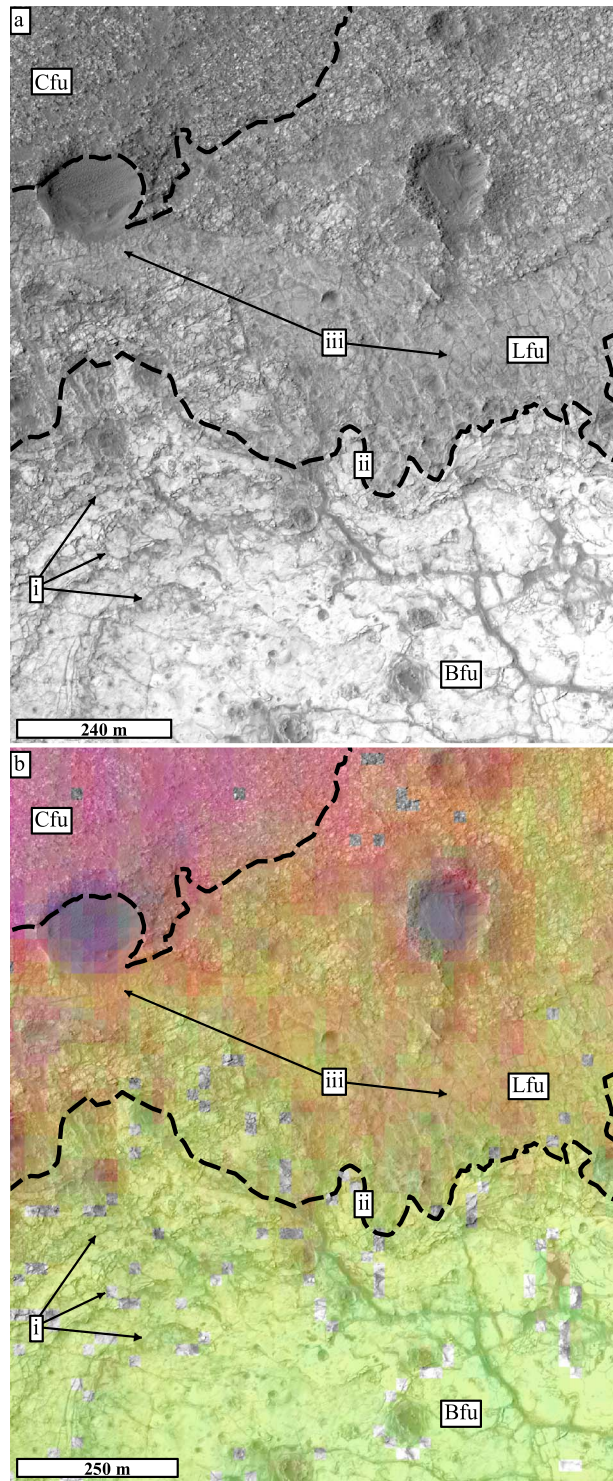


**Figure 7.** HiRISE and CRISM representations of the boundary between the bright fractured unit (*Bfu*), the layered floor unit (*Lfu*), and the caldera floor unit (*Cfu*). (a) HiRISE image PSP\_005684\_1890. Dashed lines show unit boundaries. Layers can be seen in the bright central lava (i), and it has a gradational upper boundary with *Lfu* (ii). The layered floor unit shows rectilinear polygonal surfaces in places (iii) but has a more distinct boundary with *Cfu*. (b) CRISM FRT000082EE\_07\_IF165L overlying the HiRISE image. Here pink colors represent olivine and pyroxenes forming basaltic compositions, and yellow represents plagioclase in the absence of iron-bearing minerals [Cheek *et al.*, 2013]. The gradational change from the plagioclase-bearing *Bfu* (“yellow”) to *Lfu* (“orange”) and the contact with the overlying basaltic *Cfu* (“pink”) can be seen. CRISM FRT000082EE\_07\_IF165L overlying HiRISE PSP\_005684\_1890.

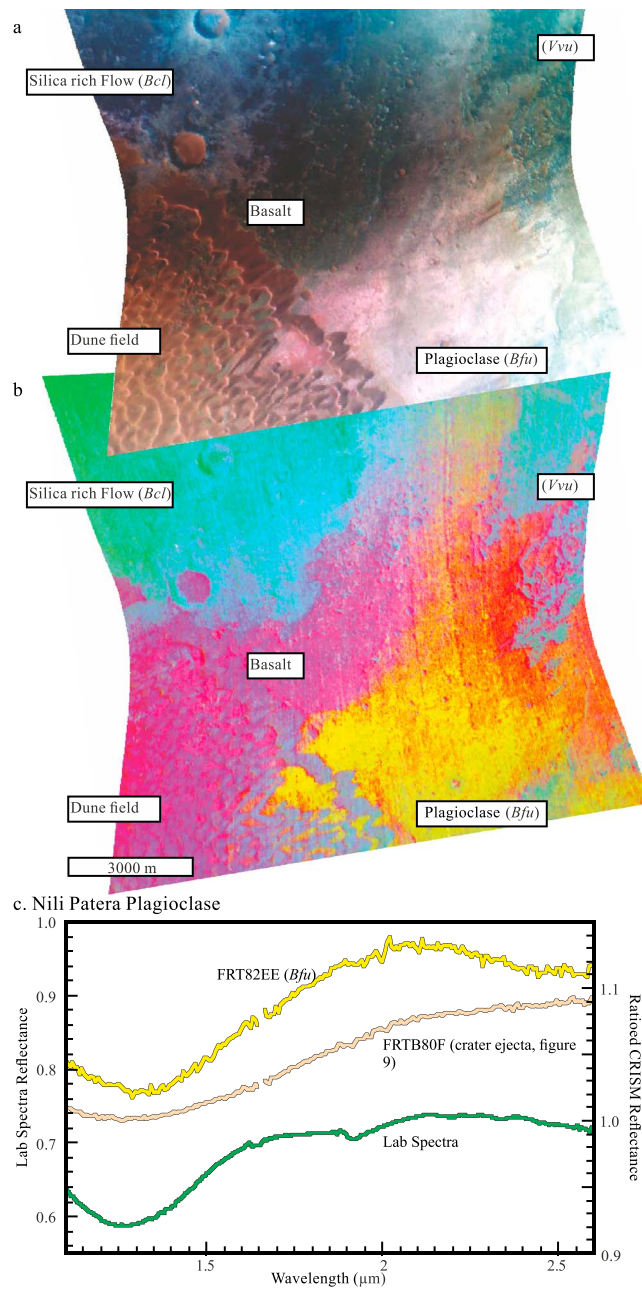


**Figure 8.** CRISM color and parameter map data from CRISM FRT000082EE, in the center of the caldera. (a) False color, map-projected CRISM image (R: 2.4 μm, G: 1.5 μm, B: 1.08 μm). (b) CRISM false color parameter map (R: Olindex, G: LCP index, B: HCP index) [Pelkey et al., 2007]. These images show clear spectral units: basalt (pink, some surfaces and the dune field), felsic (yellow, units low in the stratigraphy), and pyroxene-bearing materials (green and blue, probably other types of basaltic material). (c) Ratioed spectra from Nili Patera plagioclase deposits. FRT82EE is from the main deposit of the bright fractured unit (Bfu) in the center of the caldera [Wray et al., 2013] with a spectral average of 312 pixels centered at (119, 63) ratioed to a 1209 pixel region of interest centered at (361, 197) (CRISM: FRT000082EE). FRTB80F is less distinct, but with a still strong 1.2 μm plagioclase absorption. It is a ratio of the 1110-pixel average of light-toned material around the 1 km wide crater in Figure 9, divided by 1177 pixels of basalt to the south of the crater (CRISM: FRT0000B80F). This indicates that the pure plagioclase material is widespread and near surface. Lab spectrum is RELAB C1SC37, a 99% pure bytownite from the Stillwater Complex, Montana.

the variegated volcanic unit (Vvu; see below). The bright central lava unit is the only known silica-rich lava flow currently identified on Mars and hosts the hydrothermal silica-rich deposits mapped within Nili Patera [Skok et al., 2010a].

To the east, within this unit, is Nili Tholus (67°20'E, 9°9'N), a broadly conical edifice with an arcuate peak ridge reaching 520 m above the caldera floor (Figure 12c). This shape is suggestive of either multiple phases of construction or collapse of its eastern sector. Nili Tholus is light toned in CTX images, similar to the bright central lava unit (Bcl), and is formed of poorly consolidated, layered clastic material with clasts <2 m in size forming on slopes of ~15°. Nili Tholus appears to be part of the bright central lava unit (Bcl), but with a different surface texture, in agreement with the interpretation of Christiansen [2005]. These observations suggest a formation through the agglutination of relatively high-viscosity spatter. The foot of Nili Tholus and the bright central lava unit, Bcl, host mounds of amorphous silica (Htm; Figure 12d) as seen by Skok et al. [2010a], who consider the mounds to be derived from hydrothermal fluids driven by volcanic activity.

The northern part of the eastern caldera floor is covered by the variegated volcanic unit (Vvu). The unit consists of a bright, smooth surface to the south, which contains subcircular shallow pits, and a lower-lying, dark, rubbly surface cropping out toward the northern part of the unit and formed of rounded boulders or clasts ~2 m in diameter (Figure 13a). Both parts of this unit have features of inflated pahoehoe flows: several low shields, rift-crested ridges, lobate forms with marginal clefts (Figure 13b), and sections exposing intermittent layering of irregular

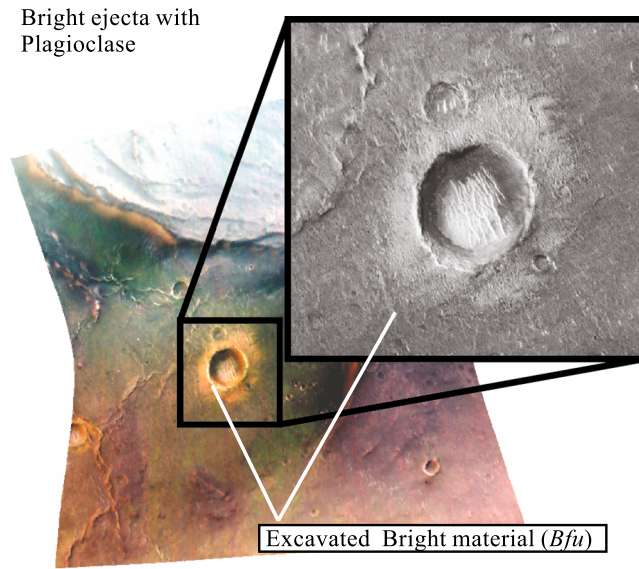


**Figure 9.** Projected CRISM (image FRT0000B80F) showing a 1 km diameter crater in eastern Nili Patera. The light-toned ejecta material strongly shows the 1.2  $\mu\text{m}$  plagioclase absorption feature. Inset shows CTX view of crater and ejecta. CTX image B19\_016905\_1890\_XN\_09N292W.

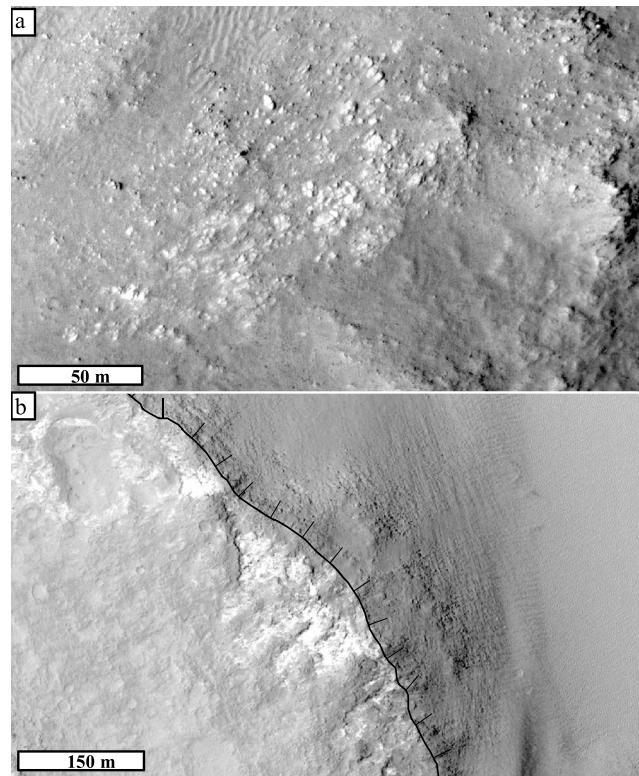


**Figure 10.** Material inferred to be part of the bright fractured unit (*Bfu*) at locations around Nili Patera: (a) in the walls of the resurgent dome axial graben (HiRISE 019595\_1890) and (b) exposed on top of the interior circumferential caldera ridges (HiRISE ESP\_027942\_1890). See Figure 5 for locations.

thickness. In addition to low shields, there are 15 possible “vent-like” mounds distributed across both textures of this unit. These are 3–4 m high, are 60–170 m in diameter, and are composed of fine-grained material and boulders up to 2 m (Figure 13a). Eight of these mounds are found within 5 km of each other. The others lie in the vicinity of reverse fault systems elsewhere in the unit. The unit has been extensively eroded, probably stripped back and mobilized by the prevailing winds, which are consistent in direction [Rafkin and Michaels, 2003] with the slip face orientations in the active dune field [Silvestro et al., 2010]. In the west, outcrops of basaltic variegated volcanic unit material cap mesas of caldera floor unit material (Figures 13c and 13d).

The final postcaldera volcanism unit (the smooth western unit; *Swu*) is characterized by strong reflectance values in the CRISM olivine parameter map (Figure 13e). The unit follows the tectonic boundary of the western caldera floor. It abuts the ridged cliffs that overly faulting in the precaldra lavas, and also the lowest parts of the domed, caldera floor unit (*Cfu*). The smooth western unit has two surface textures: smooth material making up low-lying areas and rougher material forming high stands (Figure 13f). The margins of the smooth portions of the unit form linear “high stand-like” ledges of rubbly material. These smooth areas onlap rougher protruding knobs that are spectrally consistent with adjacent units. There is a spectrally identifiable low shield, 15 m high and 400 m in diameter, in the center of the smooth western unit (Figure 13f).

In addition to the volcanic units within the caldera, there is also the intercaldera lava unit (*cl*) situated to the southeast of the

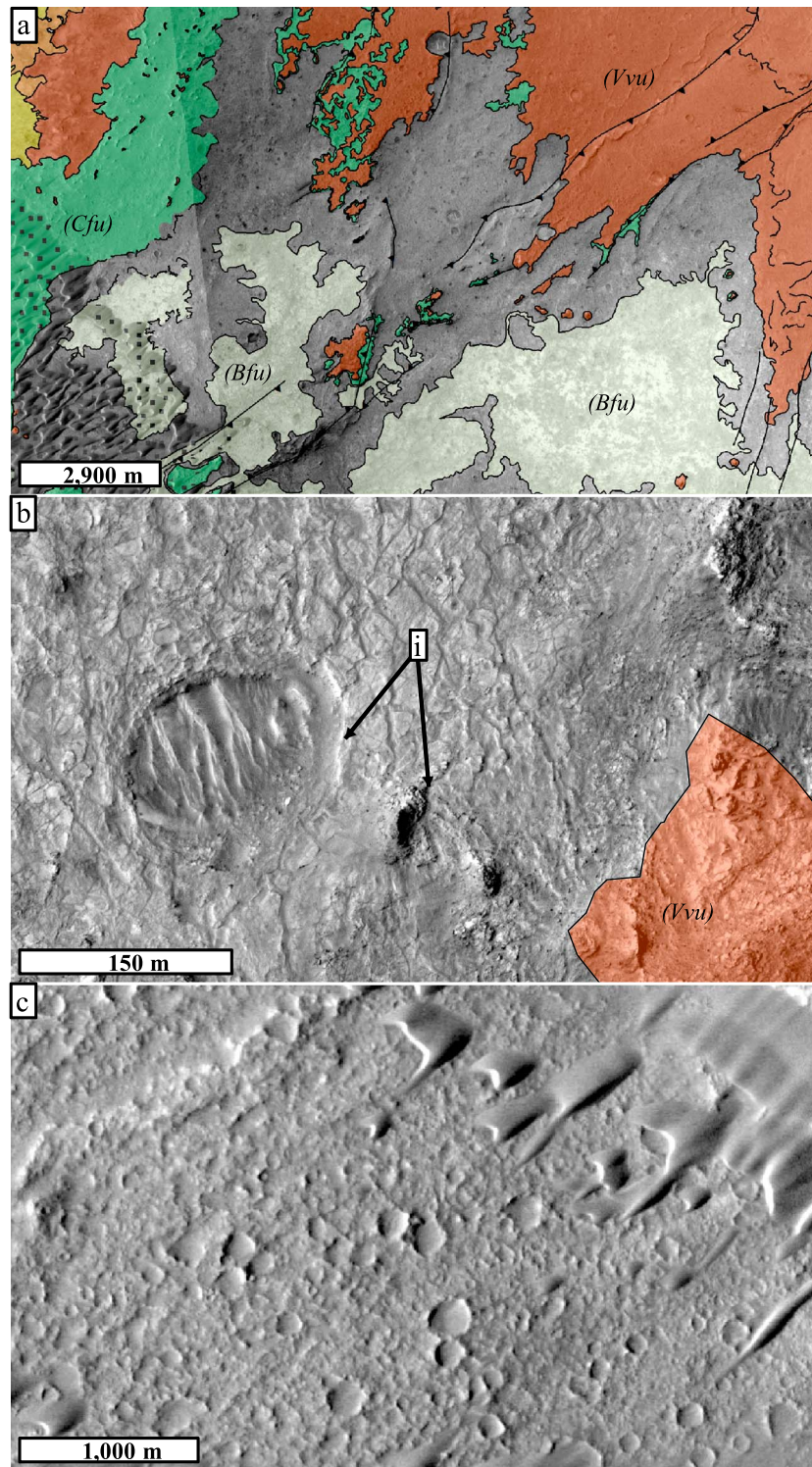


**Figure 11.** (a) The exposed surface (noncolorized areas) of the layered floor unit (*Lfu*). (b) Close-up showing (i) layering in the layered floor unit (HiRISE ESP\_018039\_1890). (c) The heavily cratered surface of the caldera floor unit (*Cfu*).

caldera, between Nili and Meroe Patera. Within this unit are channel structures and lava flows. The unit is distinguished from precaldra lavas (*Pcl*) where it overlies normal faulting within that unit. Although this unit developed contemporaneously with the postcaldera volcanism, we do not describe it in detail because it is not on the caldera floor and not strictly part of Nili Patera.

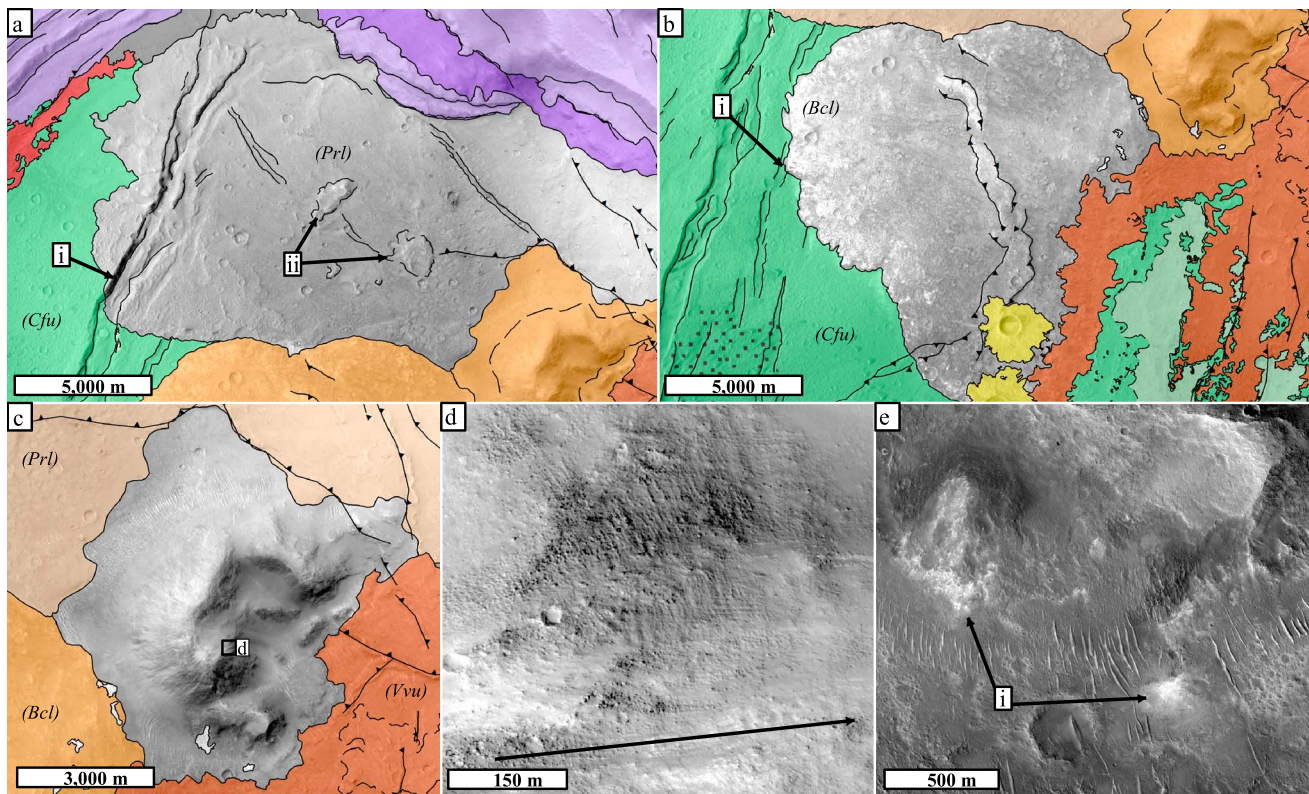


**Figure 12.** Volcanic units emplaced on the caldera floor after caldera formation. In each case, the feature being described is the noncolorized region in the scene. (a) Prerifting lava (*PrI*) (i) normal faults of the resurgent dome axis and (ii) vent mound locations. (b) Bright central lava unit (*Bcl*), (i) normal faults from the first stages of doming underlying the bright central lava unit. (c) The Nili Tholus volcanic construct. (d) Close-up view showing the layered, clastic surface of Nili Tholus (arrow shows downhill direction; HiRISE ESP\_020940\_1895). (e) Hydrothermal mounts (arrowed) at the foot of Nili Tholus (HiRISE ESP\_020940\_1895; after Skok et al. [2010a]).

### 3.2.4. Surficial Units

Across the southwest quadrant of the caldera is an area of both inactive and active dunes [Silvestro et al., 2010]. Dunes with the clearest barchan form are 300–400 m long and 25–30 m in height and show evidence of contemporaneous activity [Silvestro et al., 2010]. The dune field obscures contacts between units beneath them, although relationships can still be extrapolated by taking advantage of exposed windows between the discontinuous dune cover.

Unconsolidated surficial materials (*Usu*) mantle several areas of the caldera floor. In CTX images, this material has little tonal variation and few characteristic surface features. There are very few craters in this unit, with those few observed being <20 m across. The unit boundaries are either gradational, due to mantling, or transition into aeolian dunes.

Impact crater rim floor and ejecta materials (*I*) have been grouped together and are only mapped where the boundary is distinct or where they overlie another boundary or tectonic feature and add stratigraphic information to the map. The smallest crater mapped was ~800 m in diameter.

## 3.3. Tectonics

### 3.3.1. Normal Faulting

The earliest sets of normal faults consist of arcuate graben structures in the precaldera lavas around the circumference of Nili Patera (Figure 4). These faults are associated with subsidence around Nili Patera and the collapse to form cliffs around the disrupted lava unit (*Dcl*) and caldera floor. As a group, these faults have a maximum total throw of ~1800 m, and the curvature of their strikes defines the Nili Patera floor. Two pairs of normal faults orthogonal to the caldera rim are also part of this group of faults. This faulting trend appears to accommodate differential subsidence of the double-ridged cliff (Figure 4) around the arc of the caldera floor.

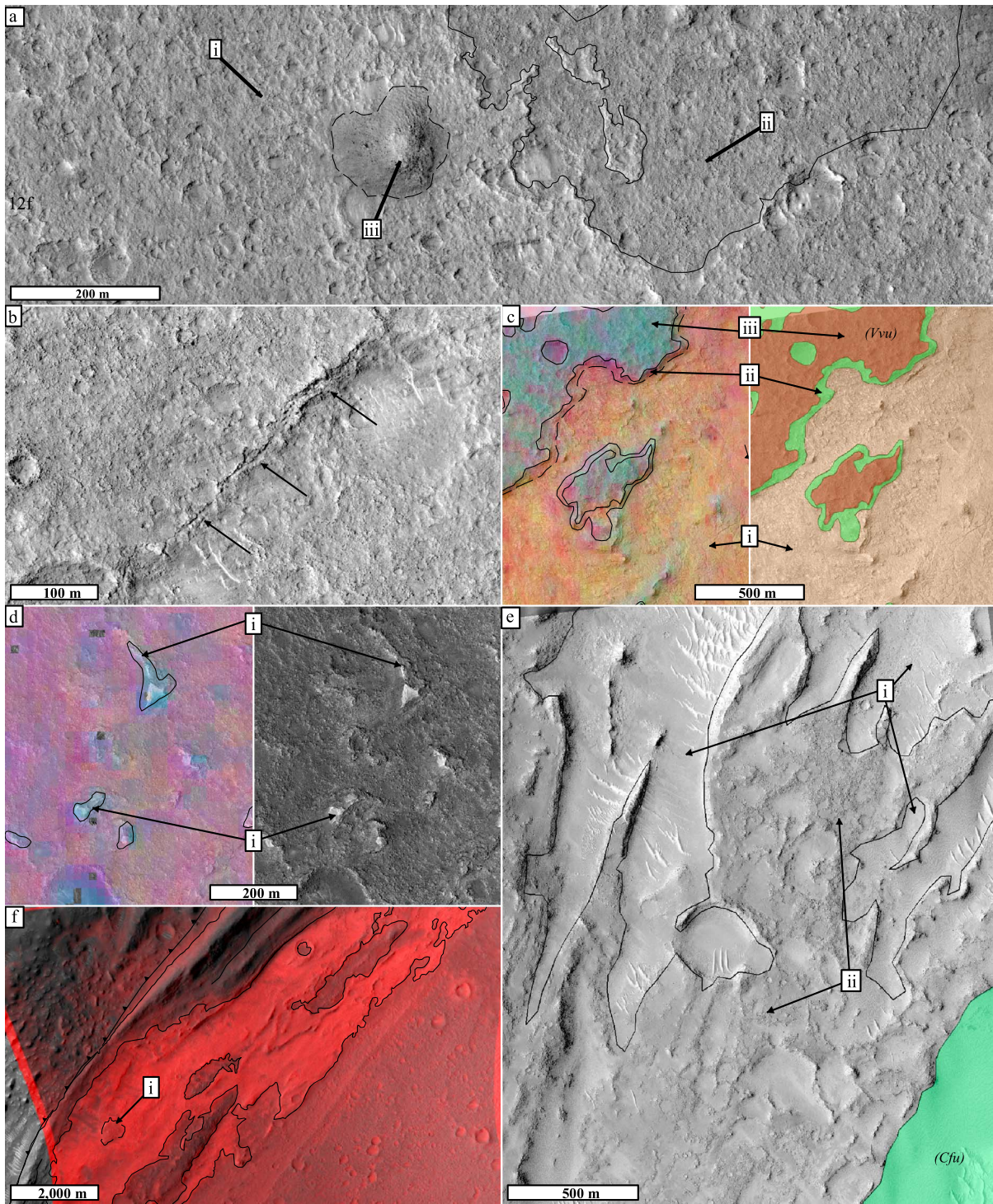


**Figure 13.** (a) Elements from the variegated volcanic unit (*Vvu*) covering the eastern portion of the caldera floor: (i) bright material, commonly higher elevation; (ii) boulders, darker material, commonly lower elevation; (iii) a low mound or cone 8 m high and 140 m wide in the variegated volcanic unit. (b) Inflation cleft (arrowed) within a pahoehoe-like lava flow axis. (c) CRISM FRT000082EE\_07\_IF165L overlain on HiRISE image PSP\_017762\_1890 (left-hand panel) showing (i) the layered floor unit (*Lfu*; spectrally “orange”) underlying (ii) the caldera floor unit (spectrally “pink”) and (iii) the variegated volcanic unit (spectrally “blue”). These areas, overlain with the false color spectral response, correspond to the geomorphically mapped units in the right-hand side of each panel. (d) CRISM FRT000082EE\_07\_IF165L overlain on HiRISE image PSP\_005684\_1890 showing (i) outliers of variegated volcanic formation (*Vvu*; spectrally “blue”) forming the caps on small mesas overlying surface material of basaltic composition in the cratered floor unit (*Cfu*). (e) The two different surface textures of the smooth western unit (*Swu*) (i) smooth surface and (ii) rough surface. (f) CRISM image FRT0000CB6F\_07\_IF165L overlying CTX mosaic showing (i) the most intense olivine parameter “red” mapping onto the smooth surface of the olivine-rich formation. See Figure 5 for the location of Figures 13e and 13f relative to each other.

The second phase of normal faulting is uplift in the western caldera floor. Fault segments extend along the crest of the ~300 m high-domed region of the floor, striking at ~017° and defining the ~90 m deep apical graben. Activity on these faults straddles the emplacement of the bright central lava unit. A set of smaller faults formed first, and these were overlain by the bright central lavas (Figure 12a). A set of larger faults, which define the apical graben and accommodate resurgent dome uplift, must have been active after the emplacement of the bright central lavas. This is because the bright central lava unit cannot have been emplaced *up* this slope and there is no evidence the flow emanated from the apical graben.

### 3.3.2. Reverse and Thrust Faults

There are reverse faults inside the double-ridged cliffs (Figure 4), which formed from rotation of precaldera lava (*Pcl*) material. These faults define the boundary of the western caldera floor. This follows faulting trends consistent with collapse into an evacuated volume [Acocella, 2007].

Reverse faults bound “wrinkle ridges” localized within the structural setting of the Nili Patera floor (Figure 4) to form a pair of conjugate wrinkle ridges. These ridges intersect at ~30°, close to the lowest point in the eastern caldera floor. The ridges are not continuous with axial wrinkle ridges of the central caldera complex (see below), outside of Nili Patera, although they do lie on a comparable trend.

“Wrinkle ridges” in the mapped area, but outside the caldera floor, crosscut nearly all other units and tectonic features, but they are also crosscut by normal faults related to collapse of the Syrtis Major central caldera complex (Figure 1b). This suggests that collapse of the Syrtis Major central caldera complex was ongoing throughout the history of tectonism associated with the formation of Nili Patera itself.

## 4. Discussion

In this section, we consider the stratigraphic, tectonic, geomorphological, and compositional observations and discuss (1) the formation of Nili Patera, (2) the emplacement of basement units, (3) volcanism within the caldera after its formation, and (4) the implications for the evolution of Syrtis Major Planum.

### 4.1. Caldera Formation

Brittle failure and caldera collapse are evident at Nili Patera. However, unlike many Martian calderas [Crumpler *et al.*, 1996], the caldera floor is asymmetric in both plan view and cross section, and the floor is lower than the majority of Syrtis Major Planum (Figures 1, 4, and 14). The caldera rim is defined by normal faulting from the southwest around to the northeast, through the highest elevation on the caldera rim. This is in stark contrast to the southeast, where a gently sloping region shows no signs of similar fault activity. This part of the caldera rim slopes upward toward the center of the Syrtis Major central caldera complex. The observed pattern of interior reverse faults, and normal faulting exterior to the caldera, broadly matches the overall structural and topographic patterns characteristic of a trapdoor-style collapse (Figure 15c) [Cole *et al.*, 2005] recorded in experimental studies and terrestrial caldera complexes [Lipman, 1984, 1997; Marti *et al.*, 1994; Acocella *et al.*, 2000; Roche *et al.*, 2000; Kennedy and Stix, 2003a, 2003b; de Silva *et al.*, 2006]. In these cases, and as seen at Nili Patera, collapse is commonly driven along an outward dipping reverse fault.

However, the collapse of Nili Patera does not appear to have been as simple as the trapdoor end-member across the whole of the present-day caldera floor. During the first phase of caldera collapse, normal faulting in the western caldera rim curved around to form an elliptical caldera floor (Figure 4), and, during the later phases, the whole area has also down-sagged to form the conjugate wrinkle ridges. The normal fault pattern, the topographic asymmetry, distribution of identifiable vents, and extent of the resurgent dome indicate that the western caldera floor is structurally distinct from the eastern caldera floor within the wider trapdoor volcanotectonic depression. There has been at least one cycle of dome formation in the western caldera, and the resurgent dome (Figure 4) may be the last in a sequence of dome formation and collapse events. This is recorded by the block rotation forming the double-ridged cliffs that define the circumference of the western caldera floor (Figures 4 and 14). Cycles of activity are common in terrestrial calderas [Lipman, 1984, 1997; Marti *et al.*, 1994; Cole *et al.*, 2005; de Silva *et al.*, 2006] and reflect volume changes in the magma reservoir system [Walter and Troll, 2001].

Because the geometry of the caldera is a reflection of the size, depth, and geometry of the magma reservoir, the observed pattern implies that the initial magma reservoir was large, shallow, and asymmetric, with a low roof aspect ratio [Acocella, 2007]. The current location of the resurgent dome suggests that this elliptical

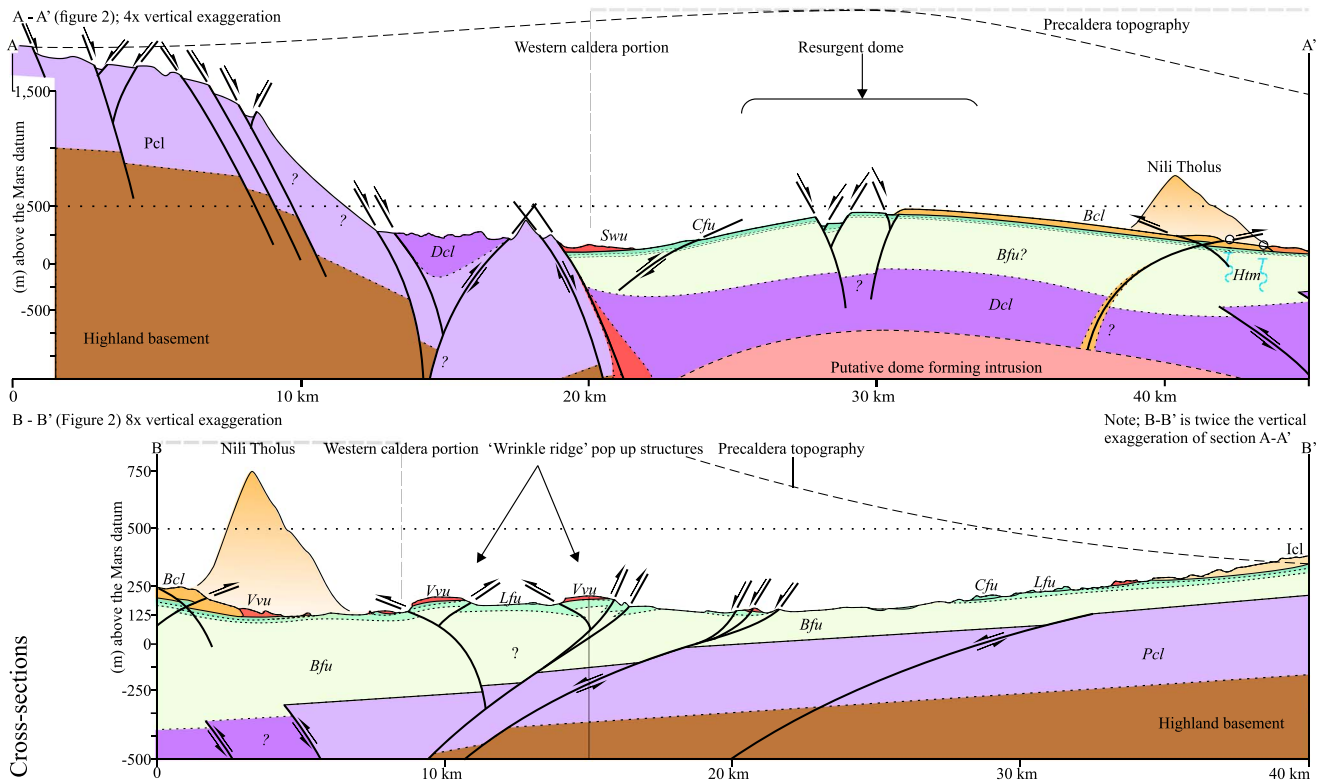


**Figure 14.** Cross section of the Nili Patera (see Figure 2 or 4 for location). Topography from CTX DTM mosaics. Section A-A' shows the western portion of the caldera at four times vertical exaggeration. Section B-B' is at eight times vertical exaggeration. The cross section shows the intracaldera ignimbrite interpretation of the bright fractured unit.

portion of the caldera was where the magma reservoir roof was thinnest and the magma reservoir was closest to the surface. Here, with a thinner caldera floor, a minimum overpressure would have permitted preferential uplift by intrusion and independent volcanotectonic development during subsequent intrusions (Figure 15d).

**4.2. Basement Emplacement**

The lowest unit of the caldera floor is the bright fractured unit (*Bfu*). This unit appears to form the basement of the caldera floor; it apparently underlies all other volcanic products and therefore is most likely to be related to other, unseen, underlying sources or to the formation of the caldera itself. The composition of this unit is unusual for Mars and correlates with a characteristic 1.2 μm absorption in the reflectance spectra, which indicates plagioclase in the absence of other significant mafic minerals. The spatial extent of the unit as mapped geomorphologically matches the extent mapped spectrally, lending support to the morphological mapping. Other units with spectrally similar characteristic units have been detected across the southern highlands of Mars, mainly in uplifted crater rims, central mounds, and sedimentary deposits [Carter and Poulet, 2013; Wray et al., 2013]. These units are considered to represent either a granitic or anorthositic intrusive body or sedimentary derivatives thereof. This sedimentary derivative interpretation is supported by the locations of the outcrops across the southern highlands. However, at Nili Patera, this material is an in situ volcanic unit and has undergone no uplift and does not contain other sedimentary features, and so we consider a sedimentary interpretation very unlikely. We now consider three alternative formation mechanisms for this bright fractured unit, and their implications for caldera formation:

1. *An exposed plutonic basement.* The first possibility is that the unit represents an intrusive body, such as the exposed upper regions of a fractionally crystallized magma reservoir exposed from under the caldera surface deposits. Modeling studies [Wray et al., 2013] show that it is plausible to form materials with the same spectral response as *Bfu* through partial melting of the material that forms the bright central lava unit (*Bcl*). This makes the assumption that the two units are genetically related and that the pluton

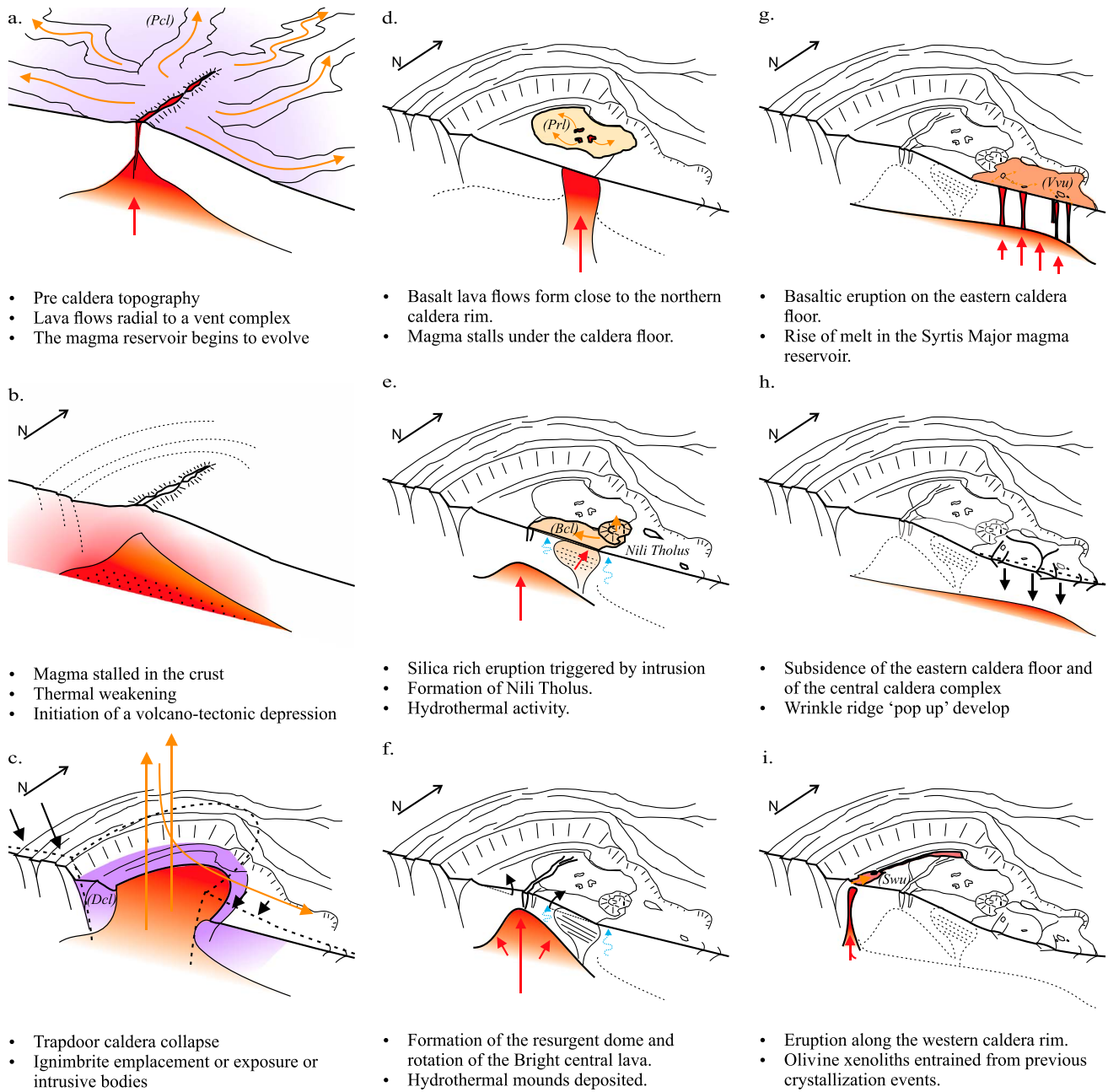


**Figure 15.** Block diagrams illustrating the volcanic history of the Nili Patera. The diagram is ~50 km wide and has five times vertical exaggeration. Arrows show the direction of travel for (orange) erupted products, (red) magma, (blue) hydrothermal fluids, and (black) tectonic or structural movement.

crystallized after the collapse of the caldera. This cogenetic scenario requires the postcollapse caldera floor to have undergone an intrusion over the 40 km wide area under the eastern caldera floor, crystallizing at a maximum of 50 m depth beneath material which has subsequently been removed through aeolian processes. There are no indicators of intrusion uplift preserved in this half of the caldera floor, arguing against a large intrusion of such shallow depth and great lateral extent.

Alternatively, the compositionally evolved, bright fractured unit could predate the caldera formation but could have been exposed latter. In this scenario, the unit crystallized before the formation of the caldera from an earlier evolved magma pulse and is thus unrelated to the *Bcl* unit. Again, a large volume of material would have had to be removed from above the pluton. Other instances of material with this composition [Carter and Poulet, 2013] have been identified in locations suggesting uplift from depth,

but the continuity of features across the caldera's peripheral fault structures suggests no substantial uplift, faulting, or removal of material in this setting. A second possibility for the exposure mechanism of the unit is that the pluton was exposed during catastrophic formation of the western caldera. A catastrophic lateral blast might have removed the substantial depth of material required to overlie a 40 km wide pluton, with the unit then being reburied to a depth of ~50 m by later eruptive products and then re-exposed by aeolian abrasion. However, there is no other geomorphic evidence for wholesale removal of material to form the shallow eastern caldera rim, and it is hard to understand how the current topography of the caldera could fit such a model, an interpretation supported by *Rogers and Nekvasil [2015]*.

2. *A welded ignimbrite basement.* The bright fractured unit might be an extrusive or explosive deposit lain down during such a catastrophic explosive event and therefore might be the remnants of a welded ignimbrite or lava. Intracaldera ignimbrites are common in terrestrial caldera complexes [*Lipman, 1984, 1997*]. An ignimbrite deposit might have been emplaced in association with the formation of the western part of the caldera and derived from an evolved magma reservoir similar to the pluton crystallization hypothesis described above. If the bright fractured unit represents lavas, then these might be associated with the silica-rich [*Christensen et al., 2005*] bright central lava unit (*Bcl*) to the north; this is considered in point 3, below. The bright fractured unit hosts a complex fracture network. The type of fracturing varies with location and depth into the unit. The fractures have a crisp morphology, and layers within the unit have been eroded to form numerous meter or submeter scale blocks (Figure 7a). These blocks have eroded out from the discontinuous layering observed in the upper part of the unit, and the layering shows gradational composition change into the overlying unit (Figure 7b). In addition, the possible outcrops of this unit in the resurgent dome and outside of the caldera reverse faults suggest that it was once a spatially extensive unit, variable in thickness and friable in its thinnest exposures. These textural features are all seen in explosive volcanic deposits such as the Tocaño and Atana ignimbrites in Chile associated with the La Pacana Caldera [*Guest, 1969; de Silva and Francis, 1989; Lindsay et al., 2001*] (Figure 16). In this analogue, the erosional exposure shows very similar sets of features as a direct consequence of its genesis. Such fabrics are all commonly seen in welded ignimbrite units, as is a vertical transition from silicic to a more mafic (greater than 5% mafic minerals in this case) composition in the upper parts of the unit that were deposited later in the eruption [*Branney and Kokelaar, 1992, 2002*]. Ignimbrites are commonly deficient in mafic minerals [*Druitt and Sparks, 1984; Gardeweg and Ramirez, 1987; Lipman, 2000*]. Eruption and emplacement mechanisms depend fundamentally on magma composition (cf. viscosity) and volatile content, although the reported composition and model partial melt from other local rocks [*Wray et al., 2013*] are consistent with this formation mechanism. This mechanism is also supported by the implied effects of volatiles. Not only will water within a magmatic system enhance the evolution of magma from a basaltic starting point toward the observed felsic composition, but volatiles also drive explosive volcanic eruptions as they are exsolved from the magma when pressure decreases. However, this hypothesis raises additional questions: was the vent (or vents) under the western part of the caldera or along the western ring fault, and how has the observed pattern of the outcrop been emplaced with respect to the trapdoor-style caldera collapse and the ensuing interpretation of asymmetric magma chamber drainage? If this unit is an ignimbrite, then the eruption that formed the deposits drove the initial stages of caldera collapse but predates the latter subsidence of the eastern caldera floor. The putative ignimbrite unit collected (and is locally thickened) in the topographic confines of the nascent central caldera complex, as well as deposited outside the caldera, but buried by subsequent volcanic resurfacing. This permitted the unit contained within the early stages of caldera subsidence to be exposed after further subsidence and erosion of the caldera floor. The preservation and topographic scenario suggest that a vent would have been beneath the western caldera floor, or more likely on the ring fault of the western caldera floor, and now either auto-obliterated or located elsewhere within the central caldera complex. Because there is no evidence to support vents elsewhere, we prefer the first suggestion: that one or more vents were located at the main reverse faults. These faults would have provided a pathway for ascending magma and driven subsidence. If a violent eruption took place in the western part of Nili Patera, this part of the caldera would likely have a weaker base to the caldera roof, where stress was concentrated during caldera formation. Consequently, it may be weaker than the eastern caldera portion, permitting preferential ascent of magma in this region during any subsequent magmatism. This is consistent with the location of the resurgent dome within the western half of the caldera [*Lipman, 1997*]. This scenario is also tectonically

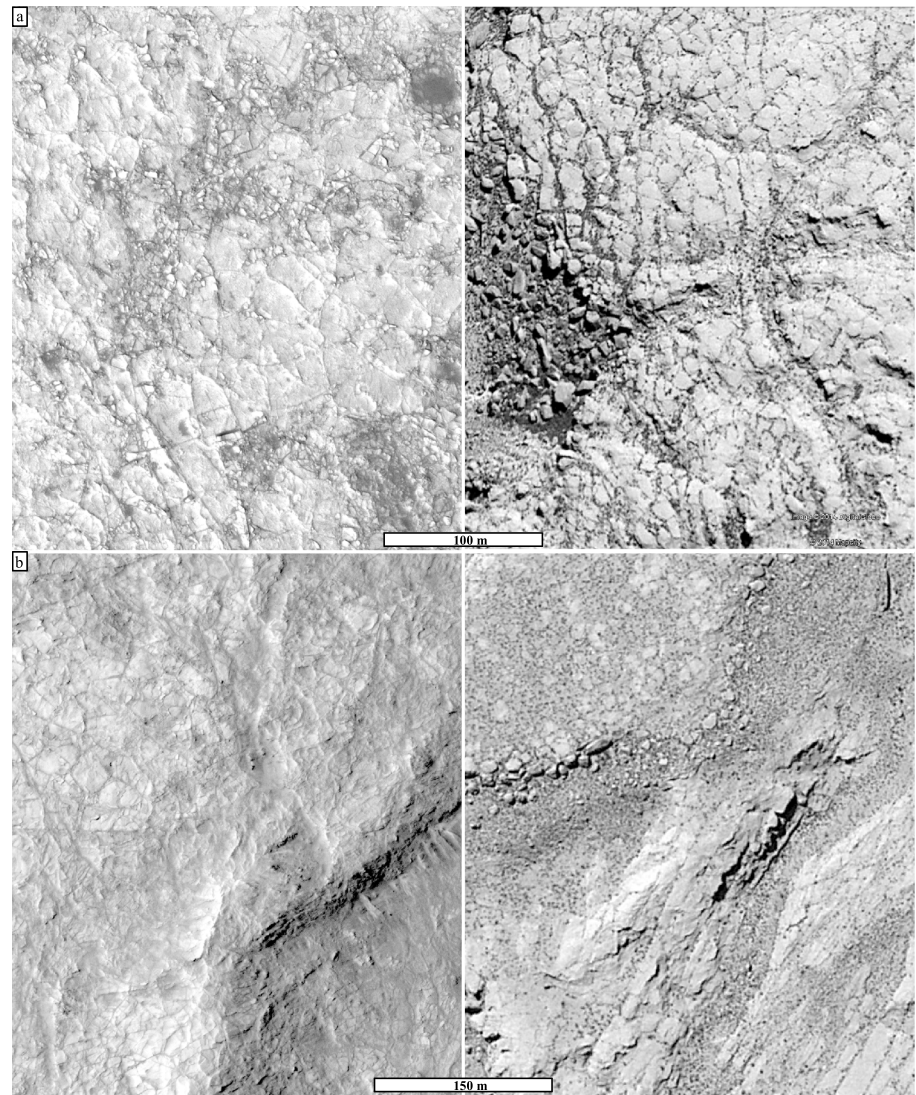


**Figure 16.** Two comparisons between locations in Late Tertiary Tocaño and Atana ignimbrites associated with the La Pacana caldera, Chile (close to  $67^{\circ}52'W$ ,  $23^{\circ}07'SN$ ; Images from Google Earth (c) 2014 CNES/Astrium), right-hand panels [Gardeweg and Ramirez, 1987; de Silva and Francis, 1989; Lindsay et al., 2001]. Locations within the Bright fractured unit (Bfu) in Nili Patera, left-hand panels. (a) Polygonal fracture patterns and blocky erosional fabric. (b) Undulating topography, internal layers and polygonal fracture patterns of the bright fractured unit (Bfu) and Atana ignimbrite.

consistent with the “butterfly body” inflections in the normal faulting, dividing the caldera into two distinct regions. The important linking implication in the two formation hypotheses presented thus far is that magmatic evolution to form differentiated intrusive or extrusive material (probably through fractional crystallization) must have occurred in the upper part of the crust beneath Syrtis Major. This interpretation is supported by the conclusions of Rogers and Nekvasil [2015], who contend that the observed mineralogy is consistent with low-pressure crystallization of residual liquids in a shallow magma chamber (after the extraction of precaldera lava materials). The third hypothesis (below) is different, in that it explores the possibility that the bright fractured unit (Bfu) is part of the effusive volcanism that postdates caldera formation.

3. *The exposed core of the silica-rich bright central lavas.* The third possibility is that the bright fractured unit is not related to caldera formation at all and is instead the same eruptive unit as the bright central lava unit. In this scenario, when the bright central lavas and the Nili Tholus formed, the lava, enriched in silica, filled the eastern portion of the caldera. Subsequently, all but the portion of the unit uplifted by the resurgent dome became buried by the overlying variegated volcanic formation (Vvu). This model would explain the

outliers of evolved composition noted by *Christensen* [2005], as well as their extent beneath the variegated volcanic unit. The compositional differences between the bright central lava unit and the bright fractured unit could be reconciled [*Horgan*, 2013] by considering the very different surface properties of the two areas: the lava surface will be very rough, with a high glass component, and will also contain aeolian material trapped into the rough surface, whereas the bright fractured unit is smooth and dust free and, probably, has a different crystal fabric. This difference can cause significant alterations in the spectral response of a surface, as measured in remote sensing data [*Serventi et al.*, 2013; *Carli et al.*, 2014a, 2014b].

However, this idea does not appear to be consistent with the stratigraphy. First, at the eastern foot of the resurgent dome, the bright fractured unit appears to underlie the cratered caldera floor unit, which in turn is seen to directly underlie the bright central lava unit, although the junction between these unit boundaries is partially obscured by dunes. Secondly, this scenario does not offer an explanation for the bright friable outliers on the interior ridges, precaldera lavas, and disrupted lava unit.

Here we have considered various mechanisms for the emplacement of the bright fractured unit, including a large explosive emplacement, the exposure of a shallow intrusion, and the differential erosion of the bright central lava unit. With the evidence available, we reject the late effusive hypothesis and consider the first two hypotheses more plausible; both derive from a fractionally crystallized magma reservoir. Given the structural, topographic, and spatial characteristics of the bright fractured unit, the welded intracaldera ignimbrite is our favored hypothesis. A final differentiation between these mechanisms might, however, only be possible with rover-scale observations of texture and geochemistry.

### 4.3. Volcanism Within Nili Patera

Since the establishment of the Nili Patera floor, it has been overprinted by several phases (both discrete and overlapping) of volcanic and tectonic events.

The first phase of events includes the formation of the northern basaltic (*Prf*) and bright central lava (*Bcl*) units with pericontemporaneous intrusion causing resurgent dome formation (Figures 15c–15f). Impact crater size frequency statistics (Table 1) show that the model ages for the *Prf* and *Bcl* units are each within the error estimates of the other. Because of the small number of visible craters and the small counting areas, strong significance cannot be placed on these absolute ages. Nevertheless, the results are consistent with these events having taken place geologically close together in time but suggest that the northern basaltic unit may be slightly older, a result supported by the mapping and inferred stratigraphy.

Stratigraphically, the first event in this phase is the emplacement of the basaltic lavas (*Prf*) and the formation of small northwest-southeast striking graben-like fault systems (Figures 12a and 15d). The faults extend into the older caldera wall units but are contemporaneous with the basalts: they crosscut the lavas but are also obscured by them closer to the vent structures which trend along the tectonic features at the eastern caldera floor structural bounds. Tectonic activity on this trend had ceased prior to the formation of Nili Tholus and the resurgent dome.

The second tectonic trend within this phase of activity, affecting these units, is associated with the resurgent dome and the formation of its axial rift (Figure 15e). Resurgent dome formation has rifted the basaltic unit and uplifted both the basaltic (*Prf*) and bright central lava units (*Bcl*). However, small faults parallel to the rift axis on the flanks of the resurgent dome are flooded by the bright central lavas (*Bcl*; Figures 12b and 15e). Therefore, these faults must have formed before the main resurgent dome uplift event—unless the bright central lava flows formed on the flank of the resurgent dome, which we consider unlikely because of the consistent slope and lack of topographically high vents. Instead, there was uplift and rotation of the bright central lava unit due to the resurgent dome formation (Figure 15f). This implies that rifting in what was to become the resurgent dome started prior to the emplacement of the bright central lava unit, which, in turn, was emplaced before the final uplift of the western caldera floor that formed the resurgent dome.

The tectonic relationships, the change to a more silica-rich lava composition and the change in eruptive style (indicative of increased magma viscosity) all suggest that this part of the magma reservoir became partially crystallized. Because these events occurred within the dating measurement errors of each other, it is possible that the same magma reservoir produced both eruptive units and that, after the basaltic eruption (*Prf*), there was a hiatus in effusive activity, during which the magma reservoir evolved due to partial crystallization.

However, it is also possible that the magma reservoir which generated the bright central lavas (*Bcl*) was unrelated to the generation of the pririfting lava (*Prf*). Subsequently, the onset of the western caldera floor intrusion (Figures 15d and 15e) triggered the eruption of an evolved magma reservoir, leading to the bright central lava unit. The 300 m high evolved cone, Nili Tholus, in the eastern portion of the caldera, formed in association with the bright central lava unit. Taken together, this sequence of events implies significant activity in the magmatic plumbing beneath Nili Patera and the central caldera complex.

The second major phase of activity (Figures 15g–15i) occurred during an extensive time window, after the formation of the bright central lavas (*Bcl*) but before the exposure events that revealed the bright fractured unit, *Bfu* (Table 1). This phase of activity comprised two volcanotectonic events, probably separated by a period of erosion: first (*Vvu*; Figure 15g), a 10–20 m thick, flow field emanated from low shields and a number of small cones in eastern Nili Patera. The flows embay the base of the resurgent dome, onlapping the bright central lava unit (*Bcl*) flows. The unit is crosscut by the wrinkle ridge “pop-up” structures in the center of eastern Nili Patera, and by the thrusts at its margins (Figure 15h). The temporal separation, if any, of these events is unclear, but the melting event that led to lava formation did not trigger eruption of the western caldera floor resurgent dome intrusive body, suggesting that it had cooled, stabilizing the resurgent dome, before the eastern melting event that resulted in the emplacement of the variegated volcanic unit (*Vvu*). The variegated volcanic unit has experienced intense aeolian erosion, perhaps because of its location: prevailing winds across Syrtis Major from the northeast are topographically focused here. To the south, where the unit has been removed to expose the underlying bright fractured unit, a maximum of 40 m depth of material has been removed. This is evidenced by the elevation change between the *Vvu* and the window through to the surface of the wind-scoured caldera floor units.

The second eruptive unit in this phase of activity created the smooth western unit (*Swu*) on the western caldera boundary (Figure 15i). This unit is smooth, with significantly fewer craters or crater remnants than any other surface in the patera. This extrusive unit probably occurs at this location because it formed as a result of rising magma exploiting structural weakness along the caldera floor boundary faults. This positioning also supports the interpretation of the olivine-rich composition as contamination from xenoliths [Clague, 1987] entrained during migration rather than the bulk chemistry of the lava, although this cannot be definitively demonstrated. The temporal relationship between this olivine-rich extrusive event and the final phase of wrinkle ridge tectonics (pop-up structures) [Watters, 2004] in the eastern caldera floor cannot be easily assessed.

The “pop-up” structures within the eastern caldera floor consist of two ridges, intersecting at  $\sim 60^\circ$ . The ridges, and the floor between them, are uplifted relative to the topography to the west (Figures 14 and 15h). The arched ridge profile and small peripheral ridges suggest an anticline, with thrust faults at the extent of the limb (Figure 4). These faults are part of a larger trend which can be traced out of the structural bounds of Nili Patera and is colinear with similar structures to the south ( $67^\circ 23' E$ ,  $8^\circ 22' N$ ) within the wider Syrtis Major central caldera complex. We interpret these features as providing evidence that the eastern caldera floor subsided while caldera evolution continued. The mechanism for the subsidence requires a change in pressure regime under the central caldera complex as a result of a change in volume. This late stage of local subsidence may well be a tectonic expression of contraction of a cooling cumulate body at depth after the cessation of magmatic activity. Gravity studies of the wider Syrtis Major central caldera complex suggest that contraction could account for a maximum, but sizeable, 300–400 m (15–20%) of subsidence [Kiefer, 2004].

The observations and interpretations made here, pertaining to the volcanism and tectonism expressed on the caldera floor, demonstrate several episodes of activity including intrusion, eruption, and subsidence. These suggest that there was injection of melt into, or melt migration within, the Syrtis Major plumbing system throughout the evolution of Nili Patera. Not all of this melt transport is expressed extrusively. The compositionally distinctive bright central lava unit provides evidence for this magma reservoir probably having evolved in isolation from other magmatic plumbing under the wider Syrtis Major central caldera complex. Its eruption was triggered by the injection of the melt which formed the resurgent dome below the western portion of Nili Patera (Figures 15e and 15f). The episodes of crustal melt evolution were episodic and temporally and/or spatially isolated.

#### 4.4. Implications for the Evolution of Syrtis Major Planum and Highland Patera-Style Volcanoes

1. *Implications for the underlying highland crust.* The main implication of this work is that, during the late Hesperian, the crustal conditions were suitable for at least one instance of silicic melt to occur, leading to ignimbrite emplacement. *Francis and Wood* [1982] outline a mechanism by which silicic pyroclastic eruptions form. Of these, we discount kimberlites [*McGetchin and Ullrich*, 1973], melting of granite crust [e.g., *Hawkesworth et al.*, 1982], and direct magma-water interaction on the basis of caldera morphology, evidence of basaltic composition in earlier eruptive phases [*Mustard et al.*, 1993], and the morphological differences between the Syrtis Major flank deposits and the highland patera in east Hellas [*Greeley and Crown*, 1990; *Crown and Greeley*, 1993]. This leaves dehydration of hydrous minerals [e.g., *Thorpe et al.*, 1979] as the primary source for volatiles and differentiation within a large magma chamber as the driver of compositional changes in this magmatic system. Of these mechanisms, it is noted that the resulting SiO<sub>2</sub> content correlates to crustal thickness [*Coulon and Thorpe*, 1981], meaning that the crust was thickened and ground ice was less abundant at this latitude, in the late Hesperian relative to conditions during the emplacement of the true highland patera volcanoes.

A further implication of caldera formation is that hydrated minerals are abundant in the highland crust or megaregolith underlying Syrtis Major Planum. Nili Patera and the central caldera complex have undergone continual deformation by subsidence throughout their evolution. Most of the volume loss as erupted products happened at the beginning of the caldera's history. However, subsidence also occurred after the formation of the caldera across the wider Syrtis Major central caldera complex area (Figure 1). Volume has therefore been lost from the caldera system, evidenced by subsidence, both during and after the major eruptive events. Caldera subsidence greater than the volume of erupted units can result from the deformation of a pseudoviscous complex within the edifice [*Roche et al.*, 2000; *Merle et al.*, 2010]. In this case, Nili Patera might be considered a "hydrothermal" caldera [*Merle et al.*, 2010]. This in turn implies that the core of Syrtis Major comprises material more ductile and deformable than the surface lavas, such as an ice-rich décollement [*Mangold et al.*, 1998], because the deformation was ongoing significantly after the time when thermomechanical weakening would have permitted ductile deformation associated with magmatic processes. This inference is additionally supported (i) by the required availability of crustal water to form hydrothermal deposits within Nili Patera [*Skok et al.*, 2010a] and (ii) by spectral evidence of a hydrated mineral assemblage (underlying the Syrtis Major peripheral lavas) recording environmental change [*Skok et al.*, 2010b; *Ehlmann and Mustard*, 2012; *Carter et al.*, 2015]. These hydrated mineral assemblages have been suggested to form a continuously deformable layer beneath Syrtis Major [*Glotch and Rogers*, 2013; *Schwegman et al.*, 2015] from which evolved compositions have been excavated [*Bandfield*, 2006], a conclusion consistent with the style of caldera formation. We suggest that repeated intrusion, assimilation, and partial melting of a ductile, hydrated Noachian highland crust drove magmatic evolution toward the compositions observed now at Nili Patera. The same processes drove caldera formation and caused the caldera to develop its position within, or below, the edifice.

2. *Implications for habitability.* The volcanic activity within Nili Patera continued longer than suggested by the formation age of Syrtis Major based on global mapping [*Tanaka et al.*, 2014], an observation consistent with dating of individual flows on Syrtis Major's flanks [*Platz et al.*, 2014]. This implies long-lived, intermittent magmatic processes and a supply of melt (and an associated, elevated geothermal gradient) over an interval of ~0.5–1 Ga. Although the duration and episodicity of volcanism are poorly constrained, in combination with the inference of a hydrous subsurface, this has important implications for subsurface habitability. Deposits within Nili Patera may provide access into a habitable enclave, formed in the Noachian crust, maintained by volcanically driven hydrothermal circulation, and protected from the surface environment by the relatively thin [*Hiesinger and Head*, 2004] lava shield. Material from such a habitat might then have found its way to the surface as part of the hydrothermal deposits found in Nili Patera. These deposits could therefore contain evidence for biomarkers, if life ever existed within such a habitat, and the Nili Patera could therefore provide an important target for future exploration.
3. *Implications for highland patera-style volcanoes.* Syrtis Major Planum, containing Nili and Meroe Patera, is a volcanic plain with a central caldera complex [*Carr*, 1973; *Greeley and Spudis*, 1981; *Mouginis-Mark and Wilson*, 1992; *Plescia*, 2004]. Although Syrtis Major is dissimilar in its flank deposit morphology to Tyrrhenus and Hadriacus Montes situated to the east of Hellas [*Greeley and Crown*, 1990; *Crown and Greeley*, 1993; *Williams et al.*, 2007, 2008], its flank deposits are more similar to those of Amphitrites

Patera, situated within Melea Planum to the south of Hellas [Williams *et al.*, 2009], and to Hesperia Planum, northeast of Hellas.

Similarities between the paterae within Syrtis Major and those within Melea Planum can also be drawn in terms of topographic and spatial characteristics. The floors of the calderas (paterae) lie below the mean elevation of the volcanic plains that surround them, and the plains are crosscut by similar networks of wrinkle ridges. Crucially, each of Hesperia Planum, Malea Planum, and Syrtis Major Planum lies on the edge of giant impact structures: Hellas Planitia for Hesperia Planum and Malea Planum, and Isidis Planitia for Syrtis Major. Consequently, understanding the formation and evolution of Nili Patera has implications for the development of other volcanic edifices situated in the Martian highlands. Nili Patera is a good study example because erosion within it provides a window into Syrtis Major, whereas similar examples in Malea Planum are overprinted by periglacial landforms [Williams *et al.*, 2009]. We postulate that the highland paterae and their associated volcanic plains formed after the Martian highland crust had thickened sufficiently to inhibit magma ascent, impeding melt advection in widespread areas. However, preferential pathways remained available in crustal-scale normal faults and isostatic compensation stress structures around giant impact basins [Peterson, 1978; Schultz, 1984; Wichman and Schultz, 1989]. Hence, magma ascent was favored in zones circumferential to giant impact basins, so the highland patera-style volcanoes, along with their colocated volcanic plains, formed in these locations in the late Noachian to early Hesperian [Williams *et al.*, 2007, 2008]. This is different to other areas of the highlands, where melt would have stalled at depth, resulting in felsic intrusions now seen uplifted in impact crater rims [Wray *et al.*, 2013].

During planum-building volcanism, the raised geothermal gradient associated with the advection of hot magma to the plains-forming eruptions would have eventually resulted in conductive heating of the surrounding crust [de Silva *et al.*, 2006] and hence a reduced density contrast between melt and crust. This would have led to magma bodies stalling, and the consequent partial melting of the Noachian crust underlying the planum. These hot intrusions would have thermomechanically weakened the crust, allowing the development of calderas such as Nili Patera. By extension, the “habitable enclave” argument made for Syrtis Major Planum is also likely to be valid for the subsurface region of these other highland patera calderas.

## 5. Conclusions

1. Nili Patera formed between 3.28 (+0.80, – 0.13 Ga) and 3.1 (+0.13, –0.22) Ga. The caldera formed initially by trapdoor collapse. The caldera formed in a volcanotectonic depression caused by thermomechanical weakening of the highland crust during underlying intrusion and magma advection. Later in the caldera history, additional subsidence occurred, probably associated with a ductile subsurface layer.
2. The bright fractured unit (*Bfu*) that underlies all later volcanic units was emplaced or exposed during caldera formation. This is either exposed parts of a felsic pluton, crystallized prior to caldera collapse, or the remnants of a welded ignimbrite formed during trapdoor collapse. These processes were probably driven by volatiles. The volatiles were likely incorporated into the magma chamber by assimilation of hydrated Noachian crustal deposits and by exsolution during fractional crystallization of the magma body when stalled in the highland crust (which was thickening during the late Hesperian). Both scenarios derive from a felsic magma reservoir fed by partial melting of the Noachian highland basement.
3. There have been five episodes of volcanic activity within Nili Patera: (1) a basaltic unit erupted from tuya-like vents in the north of the caldera, (2) Nili Tholus and the bright central lava unit erupted from an isolated magma chamber, potentially triggered by the intrusion which resulted in the formation of a resurgent dome, (3) intrusion under the western caldera floor that formed a ~300 m high elliptical dome, (4) in the eastern caldera floor, a basaltic unit emplaced from a small number of small cones and shields, which has been eroded through aeolian abrasion and mobilized into the active dune field, and (5) volcanic activity located on the western caldera ring fault which has a distinct, olivine-bearing spectral signature, perhaps caused by xenoliths dredged from a crystallized magma reservoir system.
4. There is evidence for a ductile layer beneath Syrtis Major’s lava shield. Partial melting that led to evolved compositions and hydrothermal deposits implies interaction with subsurface volatiles throughout the Nili Patera’s history. The convergence of evidence for water and hydrated materials in the presence of an

elevated geothermal gradient over an extended period of time raises the possibility of a habitable environment. Such a subsurface enclave of crustal habitability would be sampled by hydrothermal deposits in Nili Patera and should be considered as an astrobiological target for future in situ exploration.

- Conclusions drawn from the exposed units at Nili Patera, and the broad similarities to the topographic and spatial distribution of other highland paterae, imply a similar causal mechanism and astrobiological potential for those edifices.

#### Acknowledgments

We thank the science and instrument teams associated with the Mars Global Surveyor, Mars Reconnaissance Orbiter, Mars Express, and Mars Odyssey missions. This work was funded by a doctoral training grant from the UK Science and Technology Facilities Council (STFC), by the British Geological Survey BUFI case studentship, and by the UK Space Agency. We thank Vitalis (UK) Ltd. for providing GeoVisionary™ 3D visualization software, Susan Conway for ArcGIS and SocetSet wizardry, and Rich Brown for valuable insight into the textures and locations of ignimbrites. We thank David Crown, Olivier Roche, and an anonymous reviewer for their detailed comments which significantly improved the manuscript. All data presented in this manuscript are freely available via the NASA Planetary Data System. CTX mosaics and topographic data are available on request from the corresponding author. C. Vye-Brown and C. Jordan publish with permission of the Executive Director of the British Geological Survey (Natural Environment Research Council, UK).

#### References

- Acocella, V. (2007), Understanding caldera structure and development: An overview of analogue models compared to natural calderas, *Earth Sci. Rev.*, *85*(3–4), 125–160, doi:10.1016/j.earscirev.2007.08.004.
- Acocella, V., F. Cifelli, and R. Funicello (2000), Analogue models of collapse calderas and resurgent domes, *J. Volcanol. Geotherm. Res.*, *104*(1–4), 81–96, doi:10.1016/S0377-0273(00)00201-8.
- Bandfield, J. L. (2006), Extended surface exposures of granitoid compositions in Syrtis Major, Mars, *Geophys. Res. Lett.*, *33*, L06203, doi:10.1029/2005GL025559.
- Bibring, J.-P., et al. (1989), Results from the ISM experiment, *Nature*, *341*, 591–592.
- Branney, M., and P. Kokelaar (1992), A reappraisal of ignimbrite emplacement: Progressive aggradation and changes from particulate to non-particulate flow during emplacement of high-grade ignimbrite, *Bull. Volcanol.*, *54*(6), 504–520, doi:10.1007/BF00301396.
- Branney, M. J., and B. P. Kokelaar (2002), *Pyroclastic Density Currents and the Sedimentation of Ignimbrites*, Geological Society, London.
- Carli, C., M. Ciarniello, F. Capaccioni, G. Serventi, and M. Sgavetti (2014a), Spectral variability of plagioclase–mafic mixtures (2): Investigation of the optical constant and retrieved mineral abundance dependence on particle size distribution, *Icarus*, *235*(0), 207–219, doi:10.1016/j.icarus.2014.03.022.
- Carli, C., G. Serventi, and M. Sgavetti (2014b), VNIR spectral characteristics of terrestrial igneous rocks: Mineralogical composition and the influence of texture, *Geol. Soc. London Spec. Publ.*, *401*, doi:10.1144/SP401.19.
- Carr, M. H. (1973), Volcanism on Mars, *J. Geophys. Res.*, *78*(20), 4049–4062, doi:10.1029/JB078i020p04049.
- Carter, J., and F. Poulet (2013), Ancient plutonic processes on Mars inferred from the detection of possible anorthositic terrains, *Nat. Geosci.*, *6*(12), 1008–1012, doi:10.1038/ngeo1995.
- Carter, J., D. Loizeau, N. Mangold, F. Poulet, and J.-P. Bibring (2015), Widespread surface weathering on early Mars: A case for a warmer and wetter climate, *Icarus*, *248*(0), 373–382, doi:10.1016/j.icarus.2014.11.011.
- Cheek, L. C., K. L. Donaldson Hanna, C. M. Pieters, J. W. Head, and J. L. Whitten (2013), The distribution and purity of anorthosite across the Orientale basin: New perspectives from Moon Mineralogy Mapper data, *J. Geophys. Res. Planets*, *118*, 1805–1820, doi:10.1002/jgre.20126.
- Christensen, P. R., et al. (2005), Evidence for magmatic evolution and diversity on Mars from infrared observations, *Nature*, *436*(7050), 504–509, doi:10.1038/nature03639.
- Clague, D. (1987), Hawaiian xenolith populations, magma supply rates, and development of magma chambers, *Bull. Volcanol.*, *49*(4), 577–587, doi:10.1007/BF01079963.
- Clenet, H., P. Pinet, G. Ceuleneer, Y. Daydou, F. Heuripeau, C. Rosemberg, J.-P. Bibring, G. Bellucci, F. Altieri, and B. Gondet (2013), A systematic mapping procedure based on the modified Gaussian model to characterize magmatic units from olivine/pyroxenes mixtures: Application to the Syrtis Major volcanic shield on Mars, *J. Geophys. Res. Planets*, *118*, 1632–1655, doi:10.1002/jgre.20112.
- Cole, J. W., D. M. Milner, and K. D. Spinks (2005), Calderas and caldera structures: A review, *Earth Sci. Rev.*, *69*(1–2), 1–26, doi:10.1016/j.earscirev.2004.06.004.
- Coulon, C., and R. S. Thorpe (1981), Role of continental crust in petrogenesis of orogenic volcanic associations, *Tectonophysics*, *77*(1–2), 79–93, doi:10.1016/0040-1951(81)90162-1.
- Crown, D. A., and R. Greeley (1993), Volcanic geology of Hadriaca Patera and the eastern Hellas region of Mars, *J. Geophys. Res.*, *98*(E2), 3431–3451, doi:10.1029/92JE02804.
- Crumpler, L. S., J. W. Head, and J. C. Aubele (1996), Calderas on Mars: Characteristics, structure, and associated flank deformation, *Geol. Soc. London Spec. Publ.*, *110*(1), 307–348.
- De Silva, S., and P. W. Francis (1989), Correlation of large ignimbrites—Two case studies from the Central Andes of northern Chile, *J. Volcanol. Geotherm. Res.*, *37*(2), 133–149, doi:10.1016/0377-0273(89)90066-8.
- De Silva, S., G. Zandt, R. Trumbull, J. G. Viramonte, G. Salas, and N. Jiménez (2006), Large ignimbrite eruptions and volcano-tectonic depressions in the Central Andes: A thermomechanical perspective, *Geol. Soc. London Spec. Publ.*, *269*(1), 47–63.
- Druitt, T. H., and R. S. J. Sparks (1984), On the formation of calderas during ignimbrite eruptions, *Nature*, *310*(5979), 679–681, doi:10.1038/310679a0.
- Dufek, J., W. S. Kiefer, M. Manga, J. E. Bleacher, and R. J. Lillis (2014), Mystery of intrusion history at Syrtis Major: Clues from multiple data sets, in 45th Lunar and Planetary Science Conference, Abstract# 2135.
- Ehlmann, B. L., and J. F. Mustard (2012), An in-situ record of major environmental transitions on early Mars at Northeast Syrtis Major, *Geophys. Res. Lett.*, *39*, L11202, doi:10.1029/2012GL051594.
- Fawdon, P., M. R. Balme, C. L. Vye-Brown, D. A. Rothery, and C. J. Jordan (2013), The evolution of volcanism in Syrtis Major Planum (Mars): Drawing insight from terrestrial analogues, p. 2135, 44th Lunar and Planetary Science Conference, The Woodlands, Tex.
- Francis, P. W., and C. A. Wood (1982), Absence of silicic volcanism on Mars: Implications for crustal composition and volatile abundance, *J. Geophys. Res.*, *87*(B12), 9881–9889, doi:10.1029/JB087iB12p09881.
- Gardeweg, M., and C. Ramírez (1987), La Pacana Caldera and the Atana ignimbrite—A major ash-flow and resurgent caldera complex in the Andes of northern Chile, *Bull. Volcanol.*, *49*(3), 547–566, doi:10.1007/bf01080449.
- Glotch, T. D., and A. D. Rogers (2013), Evidence for magma-carbonate interaction beneath Syrtis Major, Mars, *J. Geophys. Res. Planets*, *118*, 126–137, doi:10.1029/2012JE004230.
- Greeley, R., and D. A. Crown (1990), Volcanic geology of Tyrrhena Patera, Mars, *J. Geophys. Res.*, *95*(B5), 7133–7149, doi:10.1029/JB095iB05p07133.
- Greeley, R., and J. E. Guest (1987), Geologic map of the eastern equatorial region of Mars.
- Greeley, R., and P. D. Spudis (1981), Volcanism on Mars, *Rev. Geophys.*, *19*(1), 13–41, doi:10.1029/RG019i001p00013.
- Guest, J. E. (1969), Upper Tertiary Ignimbrites in the Andean Cordillera of part of the Antofagasta Province, Northern Chile, *Geol. Soc. Am. Bull.*, *80*(3), 337–362, doi:10.1130/0016-7606(1969)80[337:UTIITA]2.0.CO;2.

- Hawkesworth, C. J., M. Hammill, A. R. Gledhill, P. van Calsteren, and G. Rogers (1982), Isotope and trace element evidence for late-stage intra-crustal melting in the High Andes, *Earth Planet. Sci. Lett.*, *58*(2), 240–254, doi:10.1016/0012-821X(82)90197-2.
- Hiesinger, H., and J. W. Head III (2004), The Syrtis Major volcanic province, Mars: Synthesis from Mars Global Surveyor data, *J. Geophys. Res.*, *109*, E01004, doi:10.1029/2003JE002143.
- Horgan, B. (2013), Planetary science: Evolved magma on Mars, *Nat. Geosci.*, *6*(12), 991–992, doi:10.1038/ngeo2010.
- Kennedy, B., and J. Stix (2003a), Igneous rock associations 1. Styles and mechanisms of caldera collapse, *Geosci. Can.*, *30*, doi:10.12789/gsv30i2.4144.
- Kennedy, B., and J. Stix (2003b), Igneous rock associations of Canada 2. Stages in the temporal evolution of calderas, *Geosci. Can.*, *30*, doi:10.12789/gsv30i3.4151.
- Kiefer, W. S. (2004), Gravity evidence for an extinct magma chamber beneath Syrtis Major, Mars: A look at the magmatic plumbing system, *Earth Planet. Sci. Lett.*, *222*(2), 349–361, doi:10.1016/j.epsl.2004.03.009.
- Kirk, R. L., et al. (2008), Ultrahigh resolution topographic mapping of Mars with MRO HiRISE stereo images: Meter-scale slopes of candidate Phoenix landing sites, *J. Geophys. Res.*, *113*, E00A24, doi:10.1029/2007JE003000.
- Kneissl, T., S. van Gasselt, and G. Neukum (2011), Map-projection-independent crater size-frequency determination in GIS environments—New software tool for ArcGIS, *Planet. Space Sci.*, *59*(11–12), 1243–1254, doi:10.1016/j.pss.2010.03.015.
- Lindsay, J. M., A. K. Schmitt, R. B. Trumbull, S. De Silva, W. Siebell, and R. Emmermann (2001), Magmatic evolution of the La Pacana Caldera system, Central Andes, Chile: Compositional variation of two cogenetic, large-volume felsic ignimbrites, *J. Petrol.*, *42*(3), 459–486, doi:10.1093/ptrology/42.3.459.
- Lipman, P. W. (1984), The roots of ash flow calderas in western North America: windows into the tops of granitic batholiths, *J. Geophys. Res.*, *89*(B10), 8801–8841, doi:10.1029/JB089iB10p08801.
- Lipman, P. W. (1997), Subsidence of ash-flow calderas: Relation to caldera size and magma-chamber geometry, *Bull. Volcanol.*, *59*(3), 198–218.
- Lipman, P. W. (2000), Central San Juan caldera cluster: Regional volcanic framework, *Spec. Pap. Geol. Soc. Am.*, *346*, 9–70.
- Malin, M. C., et al. (2007), Context Camera investigation on board the Mars Reconnaissance Orbiter, *J. Geophys. Res.*, *112*, E05S04, doi:10.1029/2006JE002808.
- Mangold, N., P. Allemand, and P. G. Thomas (1998), Wrinkle ridges of Mars: Structural analysis and evidence for shallow deformation controlled by ice-rich décollements, *Planet. Space Sci.*, *46*(4), 345–356, doi:10.1016/S0032-0633(97)00195-5.
- Marti, J., G. J. Ablay, L. T. Redshaw, and R. S. J. Sparks (1994), Experimental studies of collapse calderas, *J. Geol. Soc.*, *151*(6), 919–929, doi:10.1144/gsjgs.151.6.0919.
- McEwen, A. S., et al. (2007), Mars Reconnaissance Orbiter's High Resolution Imaging Science Experiment (HiRISE), *J. Geophys. Res.*, *112*, E05S02, doi:10.1029/2005JE002605.
- McGetchin, T. R., and G. W. Ullrich (1973), Xenoliths in Maars and Diatremes with inferences for the Moon, Mars, and Venus, *J. Geophys. Res.*, *78*(11), 1833–1853, doi:10.1029/JB078i011p01833.
- McGuire, P. C., et al. (2009), An improvement to the volcano-scan algorithm for atmospheric correction of CRISM and OMEGA spectral data, *Planet. Space Sci.*, *57*(7), 809–815, doi:10.1016/j.pss.2009.03.007.
- Merle, O., S. Barde-Cabusson, and B. Wyk de Vries (2010), Hydrothermal calderas, *Bull. Volcanol.*, *72*(2), 131–147, doi:10.1007/s00445-009-0314-6.
- Meyer, J. D., and M. J. Grolrier (1977), Geological map of the Syrtis Major quadrangle.
- Michael, G. G., and G. Neukum (2010), Planetary surface dating from crater size-frequency distribution measurements: Partial resurfacing events and statistical age uncertainty, *Earth Planet. Sci. Lett.*, *294*(3–4), 223–229, doi:10.1016/j.epsl.2009.12.041.
- Mouginis-Mark, P. J., and L. Wilson (1992), The physical volcanology of Mars, in *Mars*, edited by B. M. Jakosky et al., pp. 249–297, The Univ. of Ariz. Press, Tucson.
- Murchie, S., et al. (2007), Compact Reconnaissance Imaging Spectrometer for Mars (CRISM) on Mars Reconnaissance Orbiter (MRO), *J. Geophys. Res.*, *112*, E05S03, doi:10.1029/2006JE002682.
- Mustard, J. F., S. Erard, J. P. Bibring, J. W. Head, S. Hartz, Y. Langevin, C. M. Pieters, and C. J. Sotin (1993), The surface of Syrtis Major: Composition of the volcanic substrate and mixing with altered dust and soil, *J. Geophys. Res.*, *98*(E2), 3387–3400, doi:10.1029/92JE02682.
- Mustard, J. F., F. Poulet, A. Gendrin, J.-P. Bibring, Y. Langevin, B. Gondet, N. Mangold, G. Bellucci, and F. Altieri (2005), Olivine and pyroxene diversity in the crust of Mars, *Science*, *307*(5715), 1594–1597.
- Neukum, G., et al. (2004), HRSC: The high resolution stereo camera of Mars Express, *ESA Spec. Publ.*, *1240*, 1–19.
- Pelkey, S. M., et al. (2007), CRISM multispectral summary products: Parameterizing mineral diversity on Mars from reflectance, *J. Geophys. Res.*, *112*, E08S14, doi:10.1029/2006JE002831.
- Peterson, J. (1978), Volcanism in the Noachis-Hellas region of Mars, 2, in *Lunar and Planetary Science Conference Proceedings*, vol. 9, pp. 3411–3432, Pergamon Press, New York.
- Platz, T., G. Michael, K. L. Tanaka, J. A. S. Jr, and C. M. Fortezzo (2013), Crater-based dating of geological units on Mars: Methods and application for the new global geological map, *Icarus*, *225*(1), 806–827, doi:10.1016/j.icarus.2013.04.021.
- Platz, T., P. Jodowski, P. Fawdon, G. G. Michael, and K. L. Tanaka (2014), Amazonian volcanic activity at the Syrtis Major volcanic province, Mars, p. 2524, 46th Lunar and Planetary Science Conference, The Woodlands, Tex.
- Plescia, J., and R. Saunders (1979), The chronology of the Martian volcanoes, in *Lunar and Planetary Science Conference Proceedings*, vol. 10, pp. 2841–2859, Pergamon Press, New York.
- Plescia, J. B. (2004), Morphometric properties of Martian volcanoes, *J. Geophys. Res.*, *109*, E03003, doi:10.1029/2002JE002031.
- Plescia, J. B., and M. P. Golombek (1986), Origin of planetary wrinkle ridges based on the study of terrestrial analogs, *Geol. Soc. Am. Bull.*, *97*(11), 1289–1299, doi:10.1130/0016-7606(1986)97<1289:OOPWRB>2.0.CO;2.
- Rafkin, S. C. R., and T. I. Michaels (2003), Meteorological predictions for 2003 Mars Exploration Rover high-priority landing sites, *J. Geophys. Res.*, *108*(E12), 8091, doi:10.1029/2002JE002027.
- Robbins, S. J., G. D. Achille, and B. M. Hynek (2011), The volcanic history of Mars: High-resolution crater-based studies of the calderas of 20 volcanoes, *Icarus*, *211*(2), 1179–1203, doi:10.1016/j.icarus.2010.11.012.
- Roche, O., T. H. Druitt, and O. Merle (2000), Experimental study of caldera formation, *J. Geophys. Res.*, *105*(B1), 395–416, doi:10.1029/1999JB900298.
- Rogers, A. D., and H. Nekvasil (2015), Feldspathic rocks on Mars: Compositional constraints from infrared spectroscopy and possible formation mechanisms, *Geophys. Res. Lett.*, *112*, E05S04, doi:10.1002/2015GL063501.
- Schultz, P. H. (1984), Impact basin control of volcanic and tectonic provinces on Mars, in *Lunar and Planetary Science Conference*, vol. 15, pp. 728–729, Lunar and Planetary Inst., Houston, Tex.
- Schwegman, R. D., G. R. Osinski, and L. L. Tornabene (2015), Layered ejecta morphologies on Syrtis Major and implications for regional geology p. #2645, 46th Lunar and Planetary Science Conference, The Woodlands, Tex.

- Scott, D. H., and M. J. Carr (1978), Geologic map of Mars, IMAP Ser., *U.S. Geol. Surv. Misc. Invest. Map I-1083*.
- Serventi, G., C. Carli, M. Sgavetti, M. Ciarniello, F. Capaccioni, and G. Pedrazzi (2013), Spectral variability of plagioclase-mafic mixtures (1): Effects of chemistry and modal abundance in reflectance spectra of rocks and mineral mixtures, *Icarus*, 226(1), 282–298, doi:10.1016/j.icarus.2013.05.041.
- Silvestro, S., L. K. Fenton, D. A. Vaz, N. T. Bridges, and G. G. Ori (2010), Ripple migration and dune activity on Mars: Evidence for dynamic wind processes, *Geophys. Res. Lett.*, 37, L20203, doi:10.1029/2010GL044743.
- Skok, J. R., J. F. Mustard, B. L. Ehlmann, R. E. Milliken, and S. L. Murchie (2010a), Silica deposits in the Nili Patera caldera on the Syrtis Major volcanic complex on Mars, *Nat. Geosci.*, 3(12), 838–841, doi:10.1038/ngeo990.
- Skok, J. R., J. F. Mustard, S. L. Murchie, M. B. Wyatt, and B. L. Ehlmann (2010b), Spectrally distinct ejecta in Syrtis Major, Mars: Evidence for environmental change at the Hesperian-Amazonian boundary, *J. Geophys. Res.*, 115, E00D14, doi:10.1029/2009JE003338.
- Smith, D. E., et al. (2001), Mars Orbiter Laser Altimeter: Experiment summary after the first year of global mapping of Mars, *J. Geophys. Res.*, 106(E10), 23,689–23,722, doi:10.1029/2000JE001364.
- Tanaka, K. L., J. A. Skinner, J. Dohm, R. P. Irwin III, E. J. Kolb, C. M. Fortezzo, T. Platz, G. G. Michael, and T. M. Hare (2014a), Geologic map of Mars, *U.S. Geol. Surv. Sci. Invest. Map 3292*, scale 1:20,000,000, pamphlet 43 p.
- Tanaka, K. L., S. J. Robbins, C. M. Fortezzo, J. A. Skinner Jr., and T. M. Hare (2014b), The digital global geologic map of Mars: Chronostratigraphic ages, topographic and crater morphologic characteristics, and updated resurfacing history, *Planet. Space Sci.*, 95(0), 11–24, doi:10.1016/j.pss.2013.03.006.
- Thorpe, R. S., P. W. Francis, and S. Moorbath (1979), Rare earth and strontium isotope evidence concerning the petrogenesis of North Chilean ignimbrites, *Earth Planet. Sci. Lett.*, 42(3), 359–367, doi:10.1016/0012-821X(79)90044-X.
- Walter, T., and V. Troll (2001), Formation of caldera periphery faults: An experimental study, *Bull. Volcanol.*, 63(2–3), 191–203, doi:10.1007/s004450100135.
- Warner, N. H., S. Gupta, F. Calef, P. Grindrod, N. Boll, and K. Goddard (2015), Minimum effective area for high resolution crater counting of Martian terrains, *Icarus*, 245, 198–240.
- Watters, T. R. (2004), Elastic dislocation modeling of wrinkle ridges on Mars, *Icarus*, 171(2), 284–294, doi:10.1016/j.icarus.2004.05.024.
- Wichman, R., and P. Schultz (1989), Sequence and mechanisms of deformation around the Hellas and Isidis impact basins on Mars, *J. Geophys. Res.*, 94(B12), 17,333–17,357, doi:10.1029/JB094iB12p17333.
- Williams, D. A., R. Greeley, W. Zuschneid, S. C. Werner, G. Neukum, D. A. Crown, T. K. P. Gregg, K. Gwinner, and J. Raitala (2007), Hadriaca Patera: Insights into its volcanic history from Mars Express High Resolution Stereo Camera, *J. Geophys. Res.*, 112, E10004, doi:10.1029/2007JE002924.
- Williams, D. A., R. Greeley, S. C. Werner, G. Michael, D. A. Crown, G. Neukum, and J. Raitala (2008), Tyrrhena Patera: Geologic history derived from Mars Express High Resolution Stereo Camera, *J. Geophys. Res.*, 113, E11005, doi:10.1029/2008JE003104.
- Williams, D. A., et al. (2009), The Circum-Hellas Volcanic Province, Mars: Overview, *Planet. Space Sci.*, 57(8–9), 895–916, doi:10.1016/j.pss.2008.08.010.
- Wray, J. J., S. T. Hansen, J. Dufek, G. A. Swayze, S. L. Murchie, F. P. Seelos, J. R. Skok, R. P. Irwin III, and M. S. Ghiorso (2013), Prolonged magmatic activity on Mars inferred from the detection of felsic rocks, *Nat. Geosci.*, 6(12), 1013–1017, doi:10.1038/ngeo1994.
- Zurek, R. W., and S. E. Smrekar (2007), An overview of the Mars Reconnaissance Orbiter (MRO) science mission, *J. Geophys. Res.*, 112, E05S01, doi:10.1029/2006JE002701.